Computer Modeling in Engineering & Sciences

Tech Science Press

https://doi.org/10.32604/cmes.2026.081163

ARTICLE

Numerical Optimization of Internal Cooling Structure Placement for MHD Mixed Convection Using Multi-Nanoparticle Fluids

Basma Souayeh*

Department of Physics, College of Science, King Faisal University, Al-Ahsa, Saudi Arabia

*Corresponding Author: Basma Souayeh. Email: bsouayeh@kfu.edu.sa

Received: 25 February 2026; Accepted: 14 April 2026; Published: 27 May 2026

ABSTRACT: This study conducts a comprehensive numerical investigation of magnetohydrodynamic (MHD) mixed convection and entropy generation in a two-dimensional square cavity filled with a ternary hybrid nanofluid. The working fluid consists of Multi-Walled Carbon Nanotubes (MWCNT), Copper (Cu), and Ferric Oxide (Fe_3O_4) nanoparticles dispersed in water, selected for their superior thermal properties. Two vertically aligned, saw-tooth-shaped cooling structures are embedded along the left and right walls of the cavity, with four distinct configurations considered based on their vertical positioning. An externally imposed uniform magnetic field is applied to assess its influence on fluid flow, heat transfer, and thermodynamic irreversibility. The governing nonlinear partial differential equations accounting for mass, momentum, energy, and entropy generation are solved using the Finite Volume Method (FVM) in conjunction with a Full Multigrid Algorithm to enhance computational efficiency. The study systematically examines the effects of key dimensionless parameters, including the Hartmann number (Ha), Richardson number (Ri), Reynolds number (Re), nanoparticle volume fraction (φ), and structural configuration, on flow dynamics, thermal performance, and entropy generation. The results provide valuable insights into the optimization of heat transfer systems through geometrical and thermophysical enhancements under MHD conditions. Results reveal that among the configurations studied, the position (P3) configuration featuring asymmetrical placement of the internal saw-tooth cooling structures demonstrates the highest thermal performance, achieving an average Nusselt number of 63.698 at a nanoparticle volume fraction of $\varphi = 12\%$ and Richardson numbers in the range of $Ri = 60–80$. This superior performance is attributed to enhanced convective mixing and optimal disruption of thermal boundary layers without excessive entropy generation.

KEYWORDS: Mixed convection; saw-tooth internal structures; different positions; entropy analysis; triple-component nanoparticle fluid

1 Introduction

Mixed convection in enclosed cavities has garnered significant attention in recent decades due to its wide-ranging applications in thermal management systems, energy devices, and industrial processes. When combined with magnetohydrodynamic (MHD) effects, the complexity and control of heat and fluid flow within cavities become even more nuanced, especially under the influence of externally applied magnetic fields. The interplay between buoyancy-driven and forced convection mechanisms in such configurations offers a powerful means to regulate thermal performance. To further enhance the thermal transport capabilities of conventional fluids, nanotechnology has introduced nanofluids, engineered suspensions of nanoparticles with superior thermal properties [1–5]. This innovation has evolved into hybrid nanofluids, which involve combinations of two or more types of nanoparticles dispersed within a base fluid to

Copyright © 2026 The Author. Published by Tech Science Press. This work is licensed under a Creative Commons Attribution 4.0 International License, which permits unrestricted use, distribution, and reproduction in any medium, provided the original work is properly cited.

synergistically boost thermal conductivity and flow behaviour. The most advanced among these are ternary hybrid nanofluids, which incorporate three distinct nanoparticles. These fluids exhibit improved stability, enhanced thermal diffusion, and tunable thermal responses, making them highly suitable for MHD mixed convection systems in confined geometries. Qureshi et al. [6] explored the numerical simulations of MHD mixed convection of hybrid nanofluid flow in a horizontal channel with a cavity induced by an inner obstacle. The impact on heat transfer and hydrodynamic forces has been analyzed. Results revealed that between the mixed convective flow and the positive cylinder rotation, recirculating cells emerge, and as the rotation decreases, so does the size of the recirculating cells. The best heat transmission efficiency is observed for counterclockwise rotation of the cylinder. Ahmed and Raizah [7] analyzed the magnetic mixed convection of a Casson hybrid nanofluid due to split lid-driven heat generated porous triangular containers with elliptic obstacles. The major findings revealed that the cases of $UL = -1$, $UR = 1$, and cold ellipse give the highest rate of heat transfer. Armaghani et al. [8] studied the effect of source/sink heat location and size on Magneto-hydrodynamic mixed convection in a hybrid nanofluid of Al_2O_3-Cu/Water within the L-shaped cavity. The authors found that to impose the strongest magnetic field, the angles of 60 and 240 are the most effective ones. The mixed convection of Cu–water nanofluid in a porous square cavity having an isothermal solid block is analyzed numerically by Rajarathinam et al. [9] in the presence of a magnetic field. The major finding from their study is that optimum heat transfer enhancement is recorded as 4.8% at low Richardson number ($Ri = 0.01$) compared to the highest Richardson number with the increasing value of φ. Ahmed et al. [10] analyzed the mixed convection due to the movements of two perpendicular walls of an odd-shaped enclosure. The upper and right boundaries are partially heated, and several heating situations based on the positions of the active parts are considered. The authors stated that to get the best mixed convection situation, it is recommended to locate the heat sources in the middle of the outer perpendicular walls. Alqurashi et al. [11] performed a numerical study on mixed convection effect on MHD Oldroyd-B nanofluid flow over a stretching sheet through a porous medium with viscous dissipation-chemical engineering applications. Results revealed that under the influence of the coefficients of heat generation and absorption S as well as thermophoresis Nt, the concentration distribution of nanoparticles $\phi(\eta)$ becomes an increasing function. Das and Mamun [12] presented a numerical analysis of magnetohydrodynamic (MHD) mixed convection in a semicircular enclosure containing a rotating inner cylinder and filled with Al_2O_3-TiO_2-SWCNT-water nanofluids. The authors remarked that an increment of 6.98% in heat transfer for SWCNT-water nanofluid is observed from Ri = 1 to Ri = 10. Prince et al. [13] performed an analysis of the influence of the magnetic field inclination angle on magnetohydrodynamic double diffusive mixed convection for different types of ideal and hybrid nanofluids inside a lid driven trapezoidal enclosure with two spinning cylinders. The authors remarked that *SWCNT*-water shows maximum convective heat transfer. Moreover, a larger percentage of *SWCNT* and *Cu* nanoparticles in water are good for convective heat transfer.

Within MHD convective systems [14–16], researchers have extensively investigated techniques for controlling fluid flow and improving thermal efficiency. One widely adopted approach involves the incorporation of internal solid bodies or obstructions within the cavity. These structures significantly alter flow patterns and promote enhanced heat transfer rates [17–19]. The presence of such internal structures alters the thermal boundary layers and induces localized vortices, which can significantly improve convective mixing, especially in mixed convection regimes. A variety of geometrical configurations such as circular, elliptical, triangular, or square-shaped bodies, have been investigated, each contributing uniquely to the flow dynamics and thermal performance depending on their shape, size, orientation, and position. The interaction between the magnetic field and the geometric-induced flow perturbation further enriches the complexity of the heat transfer process, offering a high degree of tunability for engineering applications. An exhaustive review of studies on natural convection in enclosures with and without internal bodies of

various shapes has been performed by Pandey et al. [20]. Their review presented a detailed summary of numerical and experimental studies related to laminar natural convection in enclosures with and without internal bodies. As pretended authors found that the presence of internal bodies makes significant changes in the flow characteristics within the enclosure. Hasan and Saha [21] explored the MHD combined free-forced convection and entropy generation within a square enclosure (e.g., a nuclear reactor heat removal system) incorporating resistive heating and interior heat production. The cavity is induced by a centrally positioned rotating cylinder. Authors observed that elevating *Ri* while decreasing *Ha* or increasing both *Ri* and *N* leads to enhanced heat transfer. The magnetohydrodynamic conjugate mixed convection, Joule Heating, and entropy generation through a ferrofluid filled *T*-shaped open miniature chamber with a heat-generating circular rod are analyzed by Rupam et al. [22]. Results revealed that elevated Reynolds and Grashof numbers result in increased heat transport and reduced entropy production. Aich et al. [23] presented a comprehensive Computational Fluid Dynamics (CFD) investigation of three-dimensional magnetohydrodynamic (MHD) mixed convection of carbon nanotube (CNT)-water nanofluid within a vented rectangular cavity featuring an internal vertical rod bundle with circular, square, and triangular cross-sections. The study outcomes reveal that due to their smoother geometries, the circular rods exhibit better thermal exchange rates compared to square and triangular rods.

In addition to shape and size, the position and arrangement of internal structures within a cavity play a pivotal role in governing the overall heat and fluid flow characteristics. By altering the location of these inner bodies, it is possible to manipulate the flow circulation paths, vortex interactions, and thermal boundary layer development throughout the enclosure. Strategic placement can either enhance or suppress local convective currents, leading to significant variations in heat transfer performance. For instance, positioning an internal body near a hot wall may intensify thermal gradients, while placing it centrally or near the cold wall may lead to more symmetric or stabilized flow structures. Moreover, the asymmetrical placement of internal elements introduces directional flow bias, which is particularly impactful under inclined magnetic fields and in mixed convection regimes, where both buoyancy and forced flow effects are active. The interplay between geometry and position becomes even more pronounced in complex-shaped bodies such as finned, corrugated, or tooth-like structures, which exhibit spatially dependent flow separation and recirculation behaviors. The MHD mixed convection of nanofluids in the presence of multiple rotating cylinders in different arrangements has been explored by Daneshvar Garmroodi et al. [24]. They found that to achieve the maximum enhancement for the heat transfer rate, the use of a vertical arrangement for the cylinders is advised. Another investigation was conducted by Wang et al. [25], where they analyzed the periodic unsteady natural convection flow and heat transfer in a square enclosure containing a heated circular cylinder with different vertical locations, which was numerically studied. Their numerical results showed that the heat transfer is strongly dependent on the vertical location and the pulsating temperature of the inner cylinder. Xu et al. [26] reported a numerical investigation on double diffusive mixed convection in an open enclosure with different cylinder locations. The authors concluded that when the cylinder moves from the lower to the upper location, the occurrence of local maximal mass transfer rate turns counterclockwise. Souayeh et al. [27] conducted simulations for the three-dimensional Fe_3O_4-water nanofluid flow within a cooled cubical enclosure induced by an isothermally heated solid sphere. It was assumed that the sphere's orientation (horizontal, diagonal, vertical) and placement at ten distinct positions (P1 to P10). Authors found that the optimal position is identified as P5, corresponding to the sphere's first displacement along the diagonal direction, which may be attributed to greater stability in this region, where the flow exhibits more order.

Beyond enhancing heat transfer, modern thermal system design increasingly emphasizes thermodynamic efficiency, for which entropy generation analysis has become a vital diagnostic tool. Entropy generation, rooted in the second law of thermodynamics, quantifies the irreversibilities within a system

arising from heat transfer, fluid friction, and magnetic field interactions. In convective heat transfer problems, especially those involving MHD effects and complex geometries, entropy generation offers deeper insight into energy degradation mechanisms that are not captured by conventional thermal performance metrics alone. In systems utilizing hybrid or ternary hybrid nanofluids, the transport properties are altered significantly, thereby affecting both heat transfer rates and viscous dissipation behaviour. When such fluids are subject to mixed convection in magnetically influenced cavities, the entropy generation is further affected by factors such as the strength and direction of the magnetic field, buoyancy-to-inertia force ratio, thermal conductivity enhancement, and geometrical disturbances introduced by internal bodies. Importantly, the position and shape of these inner structures can significantly redistribute local thermal gradients and velocity profiles, thereby altering the spatial pattern and magnitude of entropy generation.

In this study, a comprehensive entropy generation analysis is conducted to evaluate the thermodynamic irreversibilities associated with mixed MHD convection of ternary hybrid nanofluids in an inclined cavity containing a vertically positioned cooled saw-tooth structure. This approach not only aids in identifying regions of high entropy production but also contributes to optimizing the geometric and thermophysical parameters for energy-efficient thermal system design. Such entropy generation assessments in convective cavity flows have been widely explored in previous works, particularly in systems incorporating magnetic fields, nanofluids, and internal structures [28–30].

Despite extensive research on MHD convection and entropy generation in nanofluid-filled cavities, most existing studies have focused on mono or binary nanofluids, conventional internal geometries, or fixed internal body positions. Furthermore, only a limited number of works have combined ternary hybrid nanofluids with mixed convection mechanisms in magnetically influenced enclosures, and even fewer have considered the effect of internal structure positioning in such scenarios. To the best of our knowledge, no previous study has investigated MHD mixed convection of ternary hybrid nanofluids (Multi-Walled Carbon Nanotubes (MWCNT), Copper (Cu), and Ferric Oxide (Fe_3O_4) nanoparticles suspended in water) in a square cavity containing two symmetrically cooled saw-tooth-shaped structures, whose vertical positions are varied under four distinct states to examine their impact on thermal performance and entropy generation. This study fills that gap by conducting a comprehensive numerical investigation that integrates advanced fluid composition (ternary hybrid nanofluids), non-standard internal geometry (saw-tooth cooling elements), and positional variation effects under mixed MHD convection. A detailed entropy generation analysis is also performed to evaluate system irreversibilities and identify thermodynamically efficient configurations.

The outcomes aim to answer several open questions:

How does the vertical placement of saw-tooth structures influence heat transfer and entropy generation under mixed MHD convection?

Which positional arrangement yields optimal thermodynamic performance?

How do the complex interactions between buoyancy, magnetic field, nanofluid properties, and geometric positioning shape the flow and thermal fields?

By addressing these questions, this study contributes new insights into the design of energy-efficient thermal systems and expands the understanding of multi-parameter effects in MHD convection with advanced nanofluids and engineered internal structures.

2 Physical Description and Mathematical Formulation

2.1 Physical Description

The physical model employed in this study is illustrated in Fig. 1 and represents four distinct configurations of a two-dimensional square cavity, where mixed convection phenomena occur. The cavity is

filled with a trihybrid magnetic nanofluid composed of MWCNT-Fe_3O_4-Cu dispersed in water (H_2O). Two internally cooled structures with saw-tooth profiles are embedded vertically along the left and right walls of the enclosure, positioned differently in each configuration. These obstacles, designed to disrupt the thermal flow field, each consist of eight uniformly shaped saw-teeth and serve as cooled elements within the domain. The saw-tooth-shaped structures extend vertically over a length of 0.38*L*. The total base width occupied by the platform is 0.3*L*, where *L* denotes the characteristic length of the cavity. Each saw tooth features a rectangular geometry with a height of 0.15*L* and a tooth width of 0.02*L*. More details about the dimensions are presented in Fig. 2. Furthermore, the mixed convection phenomena within the cavity are influenced by a uniform magnetic field. Moreover, in this study, the trihybrid nanofluid under investigation consists of a uniform dispersion of Multi-Walled Carbon Nanotubes (MWCNT), Copper (Cu), and Ferrofluid (Fe_3O_4) nanoparticles in water, which serves as the base fluid. Each type of nanoparticle is assumed to occupy an equal volume fraction within the mixture. The relevant thermophysical properties of the base fluid and nanoparticles are presented in Table 1. The analysis is carried out under several simplifying assumptions: the fluid is considered incompressible, Newtonian, and flowing in a laminar regime; the Boussinesq approximation is applied to account for density variations due to temperature differences; fluid properties are taken as constant, except for the density in the buoyancy term; thermal equilibrium is assumed between the nanoparticles and the base fluid; viscous dissipation effects are neglected due to their minimal influence compared to conduction and convection; and radiative heat transfer is considered negligible. Based on these assumptions, the governing equations for the problem are formulated and will be presented in the following section.

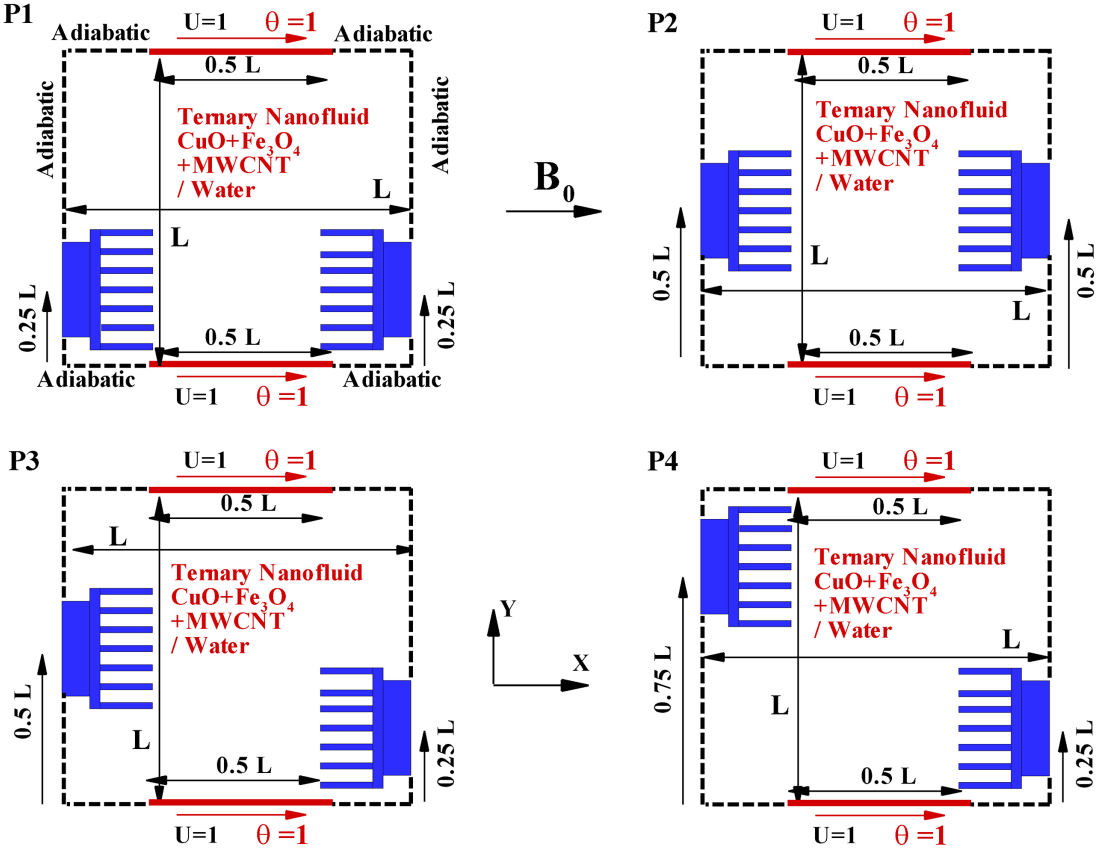

Figure 1: Physical domain depicting four variants of cooled saw-tooth structure placement within the cavity.

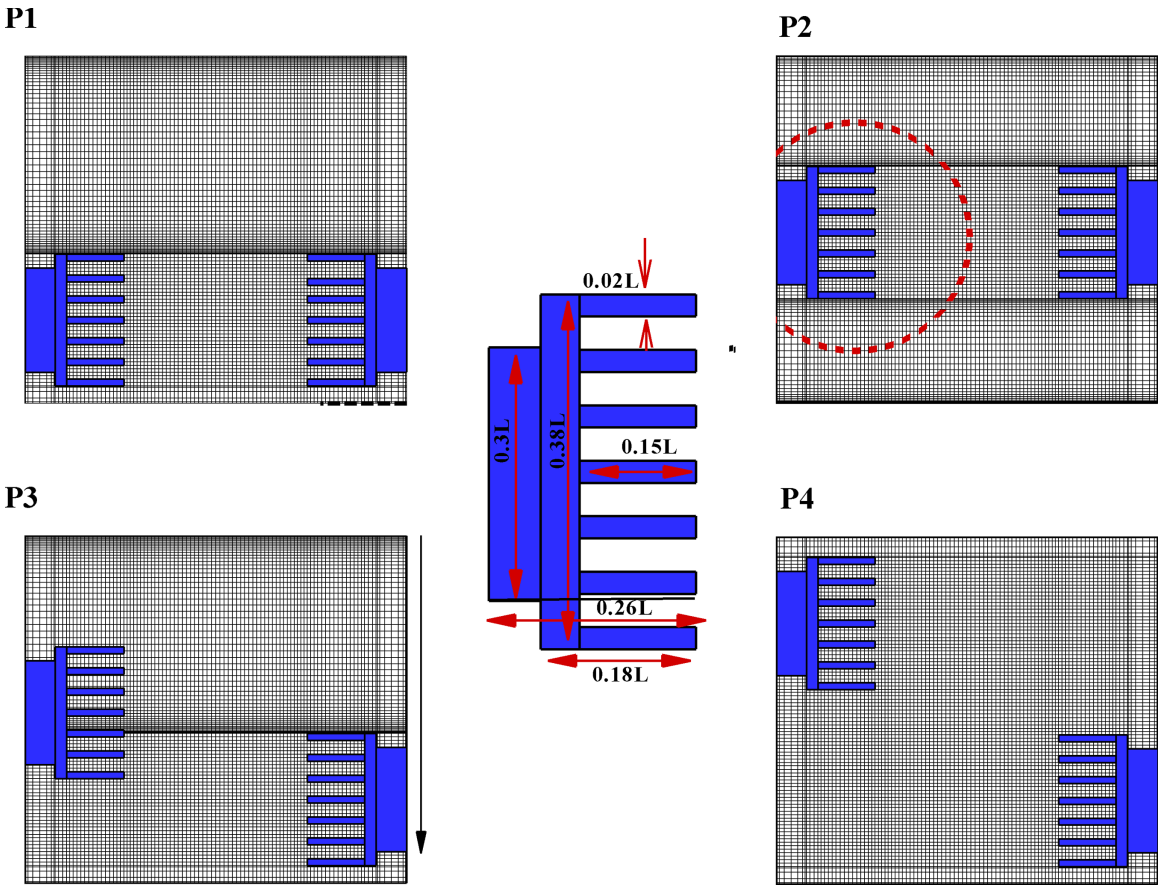

Figure 2: Discretized mesh of the computational domain.

2.2 Mathematical Formulation

2.2.1 Governing Equations

The problem under consideration involves two-dimensional, steady, and laminar fluid flow. Accordingly, the governing equations in their dimensional form, comprising the continuity equation, the x- and y-components of the momentum equations, and the energy equation for the current model, are expressed as follows [6,8,10]:

$$X = \frac{x}{L},\ Y = \frac{y}{L},\ U = \frac{u}{U_0},\ V = \frac{v}{U_0},\ P = \frac{p}{\rho_{hnf} U_0^2},\ \theta = \frac{T - T_C}{T_H - T_C},\ U_0 = \frac{\alpha_f}{L},$$

$$\Delta T = T_H - T_C,\ \mathrm{Pr} = \frac{\nu_f}{\alpha_f},\ \mathrm{Re} = \frac{U_0 L}{\nu_f},\ Ri = \frac{\beta_f g\,(T_h - T_c)\,L}{U_0^2}$$

$$\frac{\partial U}{\partial X} + \frac{\partial V}{\partial Y} = 0 \tag{1}$$

$$U\frac{\partial U}{\partial X} + V\frac{\partial U}{\partial Y} = -\frac{\rho_f}{\rho_{hnf}}\frac{\partial P}{\partial X} + \frac{\rho_f}{\rho_{hnf}}\frac{\mu_{hnf}}{\mu_f}\frac{1}{\mathrm{Re}}\left(\frac{\partial^2 U}{\partial X^2} + \frac{\partial^2 U}{\partial Y^2}\right) \tag{2}$$

$$U\frac{\partial V}{\partial X} + V\frac{\partial V}{\partial Y} = -\frac{\rho_f}{\rho_{hnf}}\frac{\partial P}{\partial Y} + \frac{\rho_f}{\rho_{hnf}}\frac{\mu_{hnf}}{\mu_f}\frac{1}{\mathrm{Re}}\left(\frac{\partial^2 V}{\partial X^2} + \frac{\partial^2 V}{\partial Y^2}\right) + \frac{(\rho\beta)_{hnf}}{\rho_{hnf}\beta_f} Ri\,\theta$$

$$-\left(\frac{\rho_f}{\rho_{hnf}}\right)\left(\frac{\Gamma_{hnf}}{\Gamma_f}\right)\frac{Ha^2}{\mathrm{Re}}V \tag{3}$$

$$U\frac{\partial\theta}{\partial X}+V\frac{\partial\theta}{\partial Y}=\frac{\alpha_{hnf}}{\alpha_f}\frac{1}{RePr}\left(\frac{\partial^2\theta}{\partial X^2}+\frac{\partial^2\theta}{\partial Y^2}\right) \tag{4}$$

To evaluate the thermophysical properties of the hybrid nanofluid, the following equations based on mixture theory are applied.

Density of trihybrid nanofluid [31]

$$\rho_{hnf}=\varphi_{MWCNT}\rho_{MWCNT}+\varphi_{Cu}\rho_{Cu}+\varphi_{Fe_3O4}\rho_{Fe_3O4}+\left(1-\varphi_{MWCNT}-\varphi_{Cu}-\varphi_{Fe_3O4}\right)\rho_f \tag{5}$$

Heat capacitance of trihybrid nanofluid [31]

$$\begin{aligned}\left(\rho C_p\right)_{hnf}&=\varphi_{MWCNT}\left(\rho C_p\right)_{MWCNT}+\varphi_{Cu}\left(\rho C_p\right)_{Cu}+\varphi_{Fe_3O4}\left(\rho C_p\right)_{Fe_3O4}\\&\quad+\left(1-\varphi_{MWCNT}-\varphi_{Cu}-\varphi_{Fe_3O4}\right)\left(\rho C_p\right)_f\end{aligned} \tag{6}$$

Buoyancy coefficient of trihybrid nanofluid

$$\begin{aligned}\left(\rho\beta\right)_{hnf}&=\varphi_{MWCNT}\left(\rho\beta\right)_{MWCNT}+\varphi_{Cu}\left(\rho\beta\right)_{Cu}+\varphi_{Fe_3O4}\left(\rho\beta\right)_{Fe_3O4}\\&\quad+\left(1-\varphi_{MWCNT}-\varphi_{Cu}-\varphi_{Fe_3O4}\right)\left(\rho\beta\right)_f\end{aligned} \tag{7}$$

Thermal conductivity of trihybrid nanofluid [32]

$$\begin{aligned}\frac{k_{hnf}}{k_f}&=\left[\frac{\varphi_{MWCNT}k_{MWCNT}+\varphi_{Cu}k_{Cu}+\varphi_{Fe_3O4}k_{Fe_3O4}}{\varphi_{hnf}}+2k_f+\right.\\&\quad\left.2\left(\varphi_{MWCNT}k_{MWCNT}+\varphi_{Cu}k_{Cu}+\varphi_{Fe_3O4}k_{Fe_3O4}\right)-2\varphi_{hnf}k_f\right]\\&\quad\times\left[\frac{\varphi_{MWCNT}k_{MWCNT}+\varphi_{Cu}k_{Cu}+\varphi_{Fe_3O_4}k_{Fe_3O4}}{\phi_{hnf}}+2k_f+\right.\\&\quad\left.2\left(\varphi_{MWCNT}k_{MWCNT}+\varphi_{Cu}k_{Cu}+\varphi_{Fe_3O4}k_{Fe_3O4}\right)+\varphi_{hnf}k_f\right]^{-1}\end{aligned} \tag{8}$$

Dynamic viscosity of trihybrid nanofluid [33]

$$\mu_{hnf}=\frac{\mu_f}{\left(1-\left(\varphi_{MWCNT}+\varphi_{Cu}+\varphi_{Fe_3O_4}\right)\right)^{2.5}} \tag{9}$$

and

$$\alpha_{hnf}=\frac{k_{hnf}}{\left(\rho C_p\right)_{hnf}} \tag{10}$$

The effective electrical conductivity of hybrid nanofluid as shown below:

$$\frac{\sigma_{hnf}}{\sigma_f} = 1+ \frac{3\left(\frac{\left(\varphi_{MWCNT}\sigma_{MWCNT} + \varphi_{Cu}\sigma_{Cu} + \varphi_{Fe_3O_4}\sigma_{Fe_3O4}\right)}{\sigma_f} - \left(\varphi_{MWCNT} + \varphi_{Cu} + \varphi_{Fe_3O_4}\right)\right)}{\left(\frac{\varphi_{MWCNT}\sigma_{MWCNT} + \varphi_{Cu}\sigma_{Cu} + \varphi_{Fe_3O_4}\sigma_{Fe_3O_4}}{\varphi_{hnf}\sigma_f} + 2\right) - \left(\frac{\varphi_{MWCNT}\sigma_{MWCNT} + \varphi_{Cu}\sigma_{Cu} + \varphi_{Fe_3O_4}\sigma_{Fe_3O_4}}{\varphi_{hnf}\sigma_f} - \left(\varphi_{MWCNT} + \varphi_{Cu} + \varphi_{Fe_3O_4}\right)\right)} \tag{11}$$

where $\varphi_{hnf} = \varphi_{MWCNT} + \varphi_{Fe_3O_4} + \varphi_{Cu}$.

Table 1: Thermophysical properties of MWCNT-Cu-Fe_3O_4/H_2O Trihybrid nanofluid [34–36].

Physical Property	MWCNT	Cu	Fe_3O_4	H_2O
$\rho\left(kg/m^3\right)$	1600	8933	5200	997.1
$C_p\left(J/kg{\cdot}K\right)$	796	385	670	4179
$k\left(w/m{\cdot}K\right)$	3000	401	6	0.613
$\beta\left(K^{-1}\right)$	4.2×10^{-5}	1.67×10^{-5}	1.3×10^{-5}	21×10^{-5}
$\Gamma\left(\Omega m\right)^{-1}$	4.8×10^{-7}	5.96×10^{-7}	25×10^{3}	0.05

2.2.2 Boundary Conditions

The four unique cases of the present model and their respective dimensionless boundary conditions are comprehensively outlined in Table 2.

Table 2: Positional configurations of cooled saw-tooth internal structures within the cavity.

Configuration	Position of First Cooled Saw-Tooth Fin	Position of Second Cooled Saw-Tooth Fin	Remarks
P1	0.25 L from the bottom on left vertical wall	0.25 L from the bottom on right vertical wall	Symmetrically placed near the cavity base
P2	0.50 L from the bottom on left vertical wall	0.50 L from the bottom on right vertical wall	Symmetrically centered
P3	0.50 L from the bottom on left vertical wall	0.25 L from the bottom on right vertical wall	Asymmetric: mid and lower positions
P4	0.75 L from the bottom on left vertical wall	0.25 L from the bottom on right vertical wall	Asymmetric: top and lower positions

Knowing that;

- All outer walls are adiabatic, i.e., no heat flux across boundaries.
- The saw-tooth structures are internally mounted structures maintained at $\theta = 1$, acting as cold sources in this study.
- The variation in vertical placement of these inner structures is the main geometric distinction affecting thermal and flow characteristics in each configuration.

2.2.3 Governing Equations for Entropy Generation Analysis

The dimensionless local entropy generation (S_T^*) is evaluated as the sum of three distinct sources of irreversibility: entropy generation due to fluid friction ($S^*_{Vis\cos ity}$), entropy generation caused by thermal gradients ($S^*_{Thermal}$), and entropy dissipation resulting from the influence of the magnetic field (S^*_{MHD}).

$$S_T^* = S^*_{Vis\cos ity} + S^*_{Thermal} + S^*_{MHD} \tag{12}$$

The mathematical expression for the entropy generation associated with fluid friction is given by:

$$S^*_{Vis\cos ity} = \chi \frac{\mu_{hnf}}{\mu_f}\left[\left(\frac{\partial U}{\partial X}\right)^2 + \left(\frac{\partial V}{\partial Y}\right)^2 + \left(\frac{\partial U}{\partial Y} + \frac{\partial V}{\partial X}\right)^2\right] \tag{13}$$

$$S^*_{Thermal} = \frac{k_{hnf}}{k_f}\left(\left(\frac{\partial \theta}{\partial X}\right)^2 + \left(\frac{\partial \theta}{\partial Y}\right)^2\right) \tag{14}$$

$$S^*_{MHD} = \chi Ha^2 \frac{\Gamma_{hnf}}{\Gamma_f}\left(U\sin\gamma - V\cos\gamma\right)^2 \tag{15}$$

where $\chi$is the irreversibility factor defined as follows:

$$\chi = \frac{\mu_f T_o}{k_f}\left(\frac{\alpha_f}{L\Delta T}\right)^2 \tag{16}$$

In all simulations, this factor is consistently set to 10^{-5}.

The dimensionless total entropy generation (S_T) is obtained by integrating the dimensionless local entropy generation (S_T^*) over the entire computational domain.

$$S_T = S_{Vis\cos ity} + S_{Thermal} + S_{MHD} \tag{17}$$

$$S_{Vis\cos ity} = \int_0^1 \int_0^1 S^*_{Vis\cos ity} dXdY \tag{18}$$

$$S_{Thermal} = \int_0^1 \int_0^1 S^*_{Thermal} dXdY \tag{19}$$

$$S_{MHD} = \int_0^1 \int_0^1 S^*_{MHD} dXdY \tag{20}$$

2.3 Heat Transfer Calculations

Optimizing the thermal performance of a system requires the simultaneous maximization of heat transfer rates and minimization of entropy generation. Accurate quantification of these thermophysical parameters is essential for establishing the theoretical limits of system efficiency. In this study, the heat transfer characteristics are assessed using the average Nusselt number, computed along the heated left wall of the cavity. Consequently, both the local and average Nusselt numbers, denoted respectively as:

$$Nu = \left.\frac{\partial \theta}{\partial n}\right|_{wall}, \quad \overline{Nu} = \frac{-k_{hnf}}{k}\int_0^1 \left.\frac{\partial \theta}{\partial X}\right|_{X=1} dY \tag{21}$$

with n representing the unit vector oriented normal to the wall.

3 Method of Solution, Grid Independence Study, and Validation

3.1 Method of Solution

In this study, we used the NASIM in-house code, developed in FORTRAN programming language [37,38] to carry out the numerical simulations. The equations were solved using the finite volume method on a staggered grid, with time integration handled by a second-order implicit Euler scheme. To reduce numerical diffusion, we applied the QUICK scheme for the advective terms [39]. Velocity and pressure were coupled using the projection method [40], which reformulates the continuity equation as a Poisson equation. This was efficiently solved with an accelerated multigrid algorithm. The remaining equations were treated using a red-black successive relaxation method [41]. At each time step, we checked for convergence using the following criterion:

$$\sum_{i,j} \left| \chi_{i,j}^{n} - \chi_{i,j}^{n-1} \right|^2 \leq 10^{-7} \tag{22}$$

where χ stands for one of the fields: velocity components u, v, the arbitrary field ϕ, or temperature θ. The index "n" indicates the iteration level, and the subscript (i, j) represents space coordinates X and Y.

3.2 Grid Independence Study

A grid independence analysis was performed to ensure the reliability of the results and determine the optimal grid resolution. The independence of the obtained results was assessed based on the expected average Nusselt number values using five different non-uniform meshes 40 × 40, 60 × 60, 80 × 80, 100 × 100, and 120 × 120 with a higher concentration of elements near solid walls. The study simulated convective heat transfer and entropy generation over the cooled inner saw-tooth structures within the square cavity filled with a trihybrid nanofluid, whose properties are listed in Table 1.

The analysis was conducted for Pr = 6.2 (for water as the base fluid), Re = 80, φ = 6%, Ha = 50, and Ri = 100 for the position P1. The goal was to identify a suitable grid size that ensures result accuracy while optimizing computational efficiency. The computed average Nusselt numbers, presented in Table 3, indicated that the 100 × 100 non-uniform grid provided a balance between accuracy and computational cost. Thus, this grid resolution was selected for all subsequent calculations.

Table 3: Average Nusselt numbers for different grid sizes at Re = 80, φ = 6%, Ha = 50, and Ri = 100 for the position P1.

Grid	40 × 40	60 × 60	80 × 80	100 × 100	120 × 120
$\overline{Nu}_{\text{North}}$	5.439	5.371	5.361	5.353	5.349
Relative Deviation (%)	–	1.25	0.18	0.14	0.08

3.3 Validation

Due to the intricate nature of the flow being analyzed, thorough validation is crucial to ensure the reliability of the proposed numerical methodology. Accordingly, the custom-developed FORTRAN code was first benchmarked against a well-established case involving two-dimensional natural convection in a differentially heated square cavity filled with Al_2O_3-water nanofluid. As shown in Table 4, the computed average Nusselt number was found to closely align with the results reported by Ghasemi et al. [42], confirming the accuracy and robustness of the present solver.

Table 4: Validation of present mean Nusselt number Results for Al_2O_3–H_2O nanofluid against Ghasemi et al. [42] at various volume fractions and Rayleigh numbers (Ha = 30).

	Ghasemi et al. [42]	Present Study	Ghasemi et al. [42]	Present Study	Ghasemi et al. [42]	Present Study	Ghasemi et al. [42]	Present Study
	$\varphi = 0$	$\varphi = 0$	$\varphi = 0.02$	$\varphi = 0.02$	$\varphi = 0.04$	$\varphi = 0.04$	$\varphi = 0.04$	$\varphi = 0.04$
$Ra = 10^3$	1.002	1.002	1.060	1.060	1.121	1.121	1.184	1.184
$Ra = 10^4$	1.183	1.181	1.212	1.231	1.249	1.283	1.291	1.338
$Ra = 10^5$	3.150	3.137	3.138	3.209	3.124	3.280	3.108	3.350
$Ra = 10^6$	7.907	7.814	7.979	7.990	8.042	8.163	8.098	8.332

4 Findings and Analysis

4.1 Effect of Fin Positioning on Thermal and Flow Characteristics of Mixed Convection Regimes

This section presents the influence of saw-tooth fin positioning on the thermo-fluidic and entropy generation characteristics in a square cavity subjected to mixed convection. The effects of varying Reynolds number (Re = 20, 40, 60, 80) on streamline, isotherm, and Bejan number contours are analyzed for four different fin configurations (P1–P4) under fixed values of Richardson number (Ri = 60), Hartmann number (Ha = 50), and nanoparticle volume fraction (φ = 6%).

Fig. 3 illustrates the streamline contours across the cavity for different configurations (P1–P4) and Reynolds numbers. At a lower Reynolds number (Re = 20), the flow is primarily buoyancy-driven, exhibiting symmetric primary vortices centered in the cavity with slight disturbances near the saw-tooth surfaces. As Re increases, the influence of forced convection becomes prominent, and stronger recirculation zones emerge. In P1, the symmetric placement of the fins at 0.25L induces symmetrical vortices that grow in intensity and complexity with increasing Re. For P2, with fins placed at mid-height (0.5L), the vortices are more organized and vertically aligned, promoting enhanced mixing in the central region. P3 and P4, which feature asymmetric fin placements, disrupt the symmetry of the flow field. Notably, P4 produces stronger secondary circulations in the lower half of the cavity due to the fin at 0.75L, encouraging more vigorous convection near the bottom cooled surface. Overall, the asymmetric positioning in P3 and P4 leads to localized enhancement in convective transport, particularly at higher Re, as the flow interacts more vigorously with the obstructions.

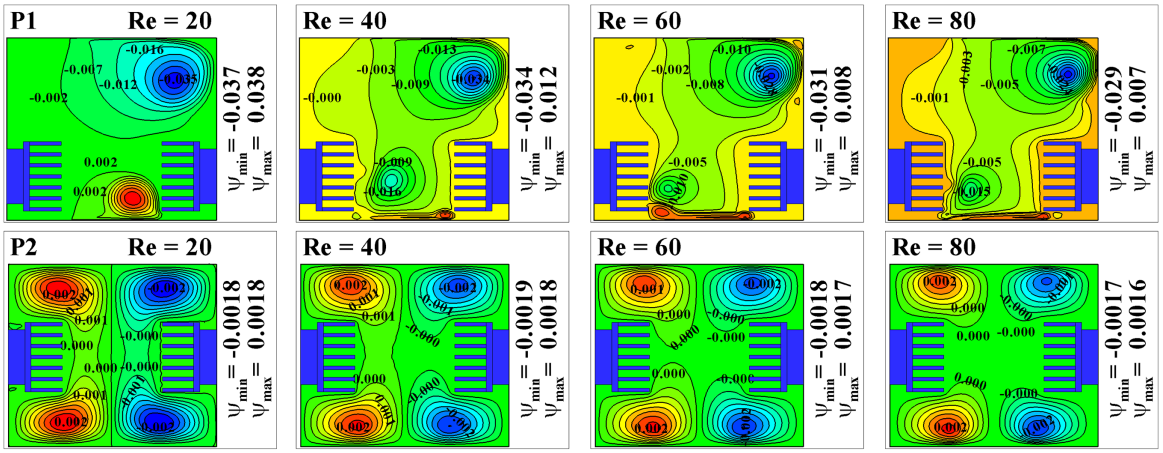

Figure 3: (Continued)

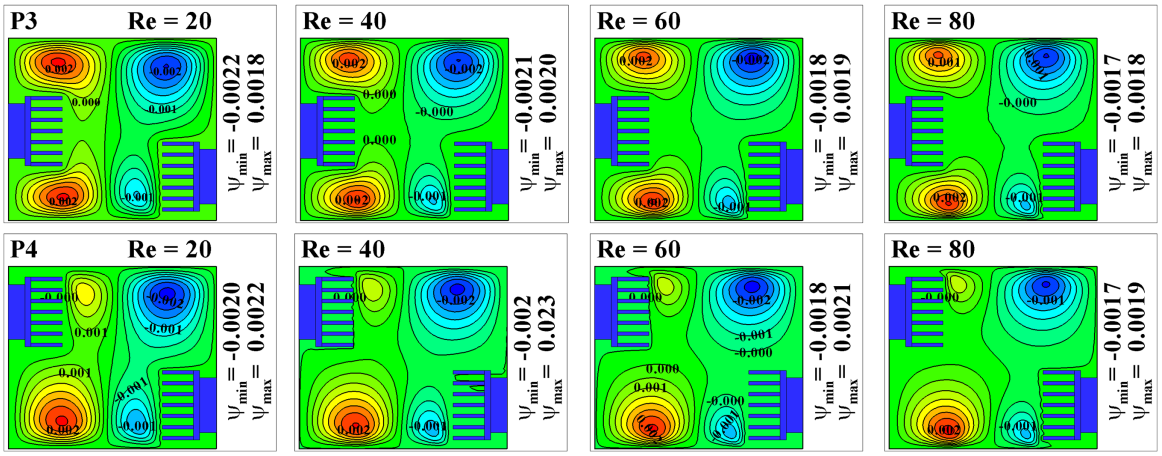

Figure 3: Streamline contours at various Reynolds numbers (*Re* = 20, 40, 60, 80) for four different saw-tooth fin configurations within the cavity, under fixed conditions of *Ri* = 60, *Ha* = 50, and φ = 6%.

Fig. 4 presents the isotherm distributions under the same range of Reynolds numbers. At *Re* = 20, heat transfer is primarily conductive, with horizontal isotherms dominating the cavity, especially in configurations P1 and P2. As Re increases, the isotherms become increasingly distorted, indicating stronger convective mixing. In P1, the symmetric cooling induces evenly distributed cold zones on both sides, with a relatively slow thermal penetration into the cavity center. P2 exhibits more efficient thermal stratification along the mid-height due to direct interference of the core flow with the cooled fins. P3 and P4 reveal more significant thermal gradient distortion, especially near the asymmetrically positioned saw-teeth. These configurations break the thermal symmetry and enhance thermal boundary layer thinning, promoting better convective heat transfer. Overall, the highest thermal mixing is observed in P4 at *Re* = 80, where both forced convection and structural-induced turbulence contribute to substantial temperature homogenization in the core region.

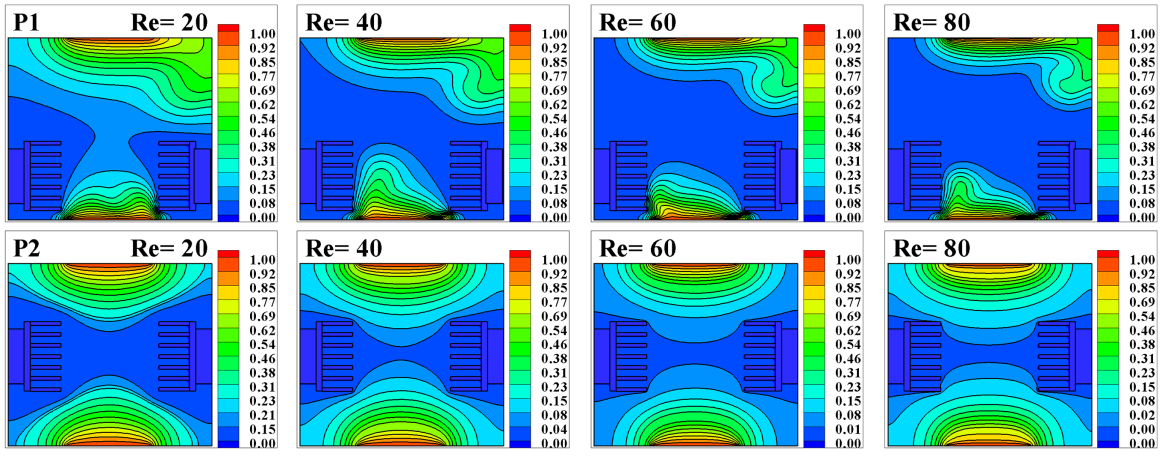

Figure 4: (Continued)

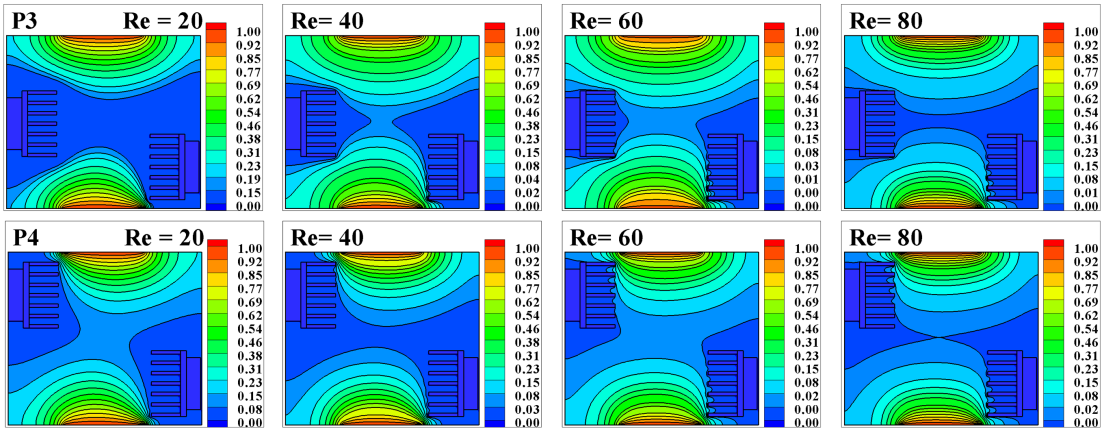

Figure 4: Isotherm contours at various Reynolds numbers (Re = 20, 40, 60, 80) for four different saw-tooth fin configurations within the cavity, under fixed conditions of Ri = 60, Ha = 50, and φ = 6%.

Fig. 5 depicts the Bejan number contours, representing the relative contributions of heat transfer irreversibility to total entropy generation. A higher Bejan number (closer to 1) indicates dominance of thermal irreversibility, whereas lower values reflect stronger viscous effects. At low Re, the Bejan number is high throughout the cavity in all configurations, suggesting that entropy is primarily generated by thermal gradients. With increasing Re, viscous dissipation grows, especially near the fins and the cavity center, where flow velocity is highest. Actually, P2 and P3 show more uniform entropy generation distribution, while P4 exhibits localized zones of low Bejan number near the bottom saw-tooth fin, signifying enhanced viscous effects. The asymmetric fin placement in P4 leads to a broader range of entropy behaviours, with distinct zones of high and low Bejan number, reflecting the strong coupling between flow structure and thermodynamic irreversibility. Overall, configuration P4 provides the most favourable mixing and entropy behaviour at higher Reynolds numbers, balancing convective heat transfer and entropy generation more effectively than other configurations.

This section presents a comprehensive analysis of the mixed convection and entropy generation characteristics within a square cavity embedded with two internal saw-tooth-shaped cooled obstacles at various vertical positions. The influence of the Richardson number (Ri = 20, 40, 60, 100) is investigated for four different positional configurations (P1–P4), with Re = 100, Ha = 50, and φ = 0.06 kept constant throughout.

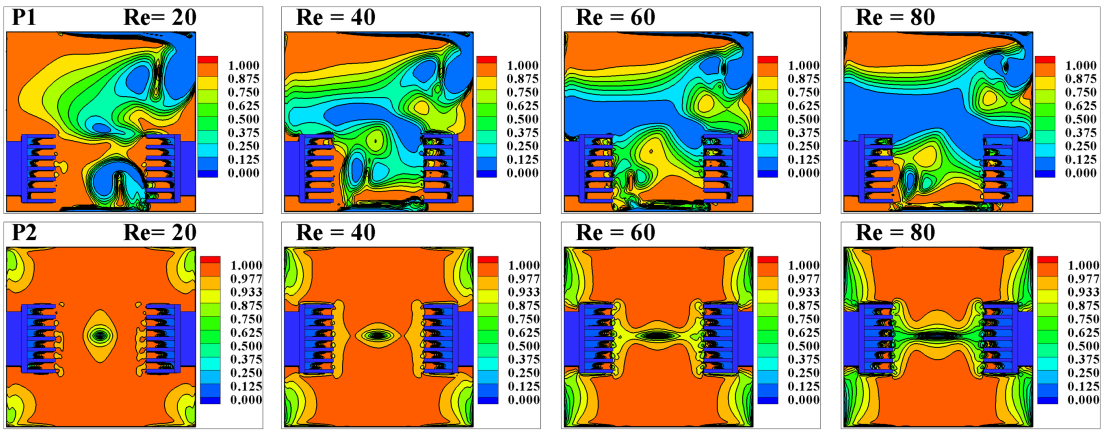

Figure 5: (Continued)

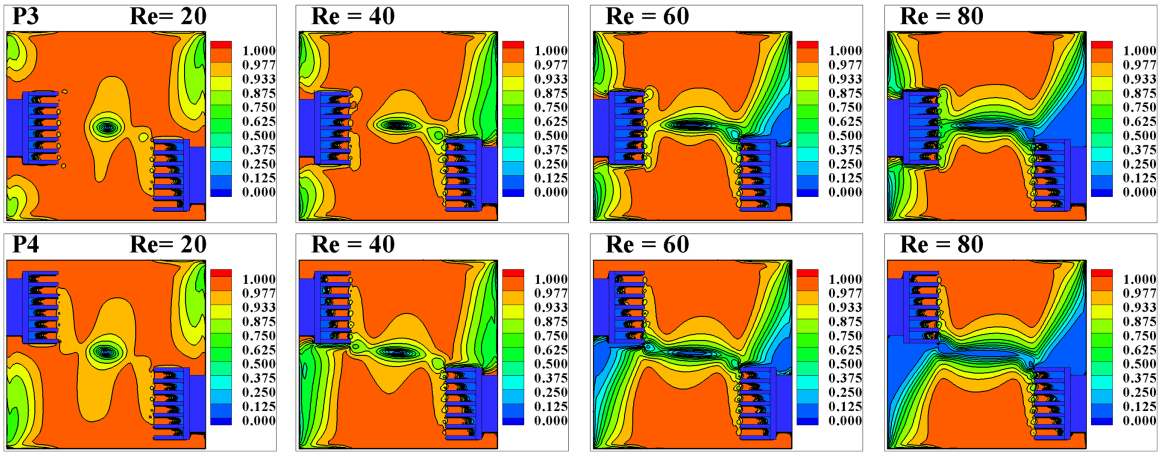

Figure 5: Bejan contours at various Reynolds numbers (*Re* = 20, 40, 60, 80) for four different saw-tooth fin configurations within the cavity, under fixed conditions of *Ri* = 60, *Ha* = 50, and φ = 6%.

Fig. 6 illustrates the streamline distributions for configurations P1–P4 at increasing Richardson numbers. At low *Ri* (*Ri* = 20), the flow is predominantly forced convection dominated, resulting in well-developed circulation cells filling the cavity. The recirculation zones are notably altered by the saw-tooth structures, with P1 and P4 showing stronger central vortices due to the symmetric and asymmetric cooling source interference. As Ri increases, buoyancy effects intensify. For *Ri* = 100, dual-cell or multicellular vortex structures emerge, especially in P2 and P3 configurations, indicating a transition to buoyancy-driven flow. The disruption caused by the different vertical positions of the cooled saw-tooth walls leads to non-uniform vortex intensity and shifting of circulation centers, which is more pronounced in P3 and P4 due to the asymmetry in obstacle placement.

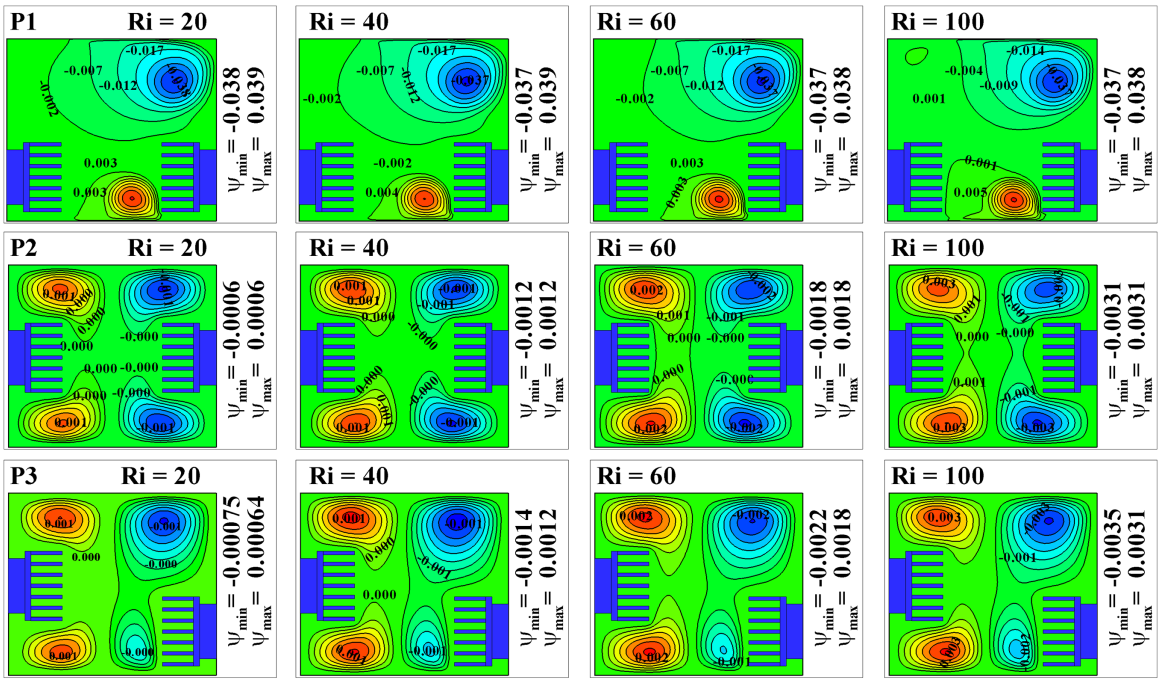

Figure 6: (Continued)

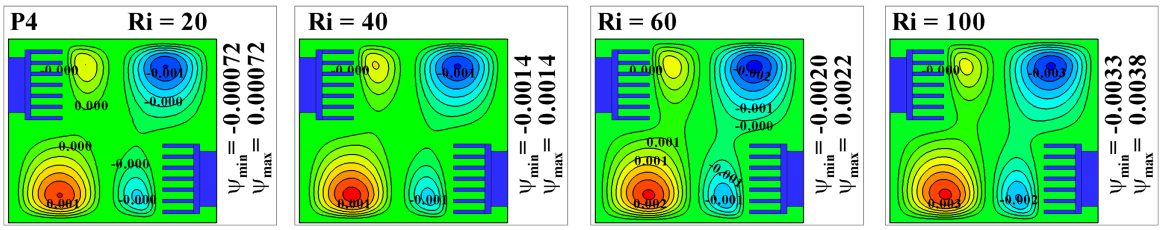

Figure 6: Streamline contours at various Richardson numbers (*Ri* = 20, 40, 60, 100) for four different saw-tooth fin configurations within the cavity, under fixed conditions of *Re* = 20, *Ha* = 50, and φ = 6%.

The isotherm distributions in Fig. 7 show the temperature gradients and thermal boundary layer development under mixed convection conditions. At *Ri* = 20, temperature contours are nearly horizontal in the core region, suggesting a dominance of conduction and weak convective mixing. As *Ri* increases, thermal stratification becomes stronger, particularly in the upper and lower regions of the cavity. Configuration P2, with both saw-tooth structures at mid-height, exhibits symmetrical thermal distribution and better thermal penetration compared to the other configurations. In contrast, P3 and P4 show asymmetrical heat dispersion, where one side remains thermally active while the other is relatively insulated due to localized recirculation and reduced convective currents. Notably, at *Ri* = 100, the cold saw-tooth structures cause strong thermal gradients near the walls, especially in P1 and P2, indicating effective heat extraction and enhanced local convection due to increased buoyancy forces.

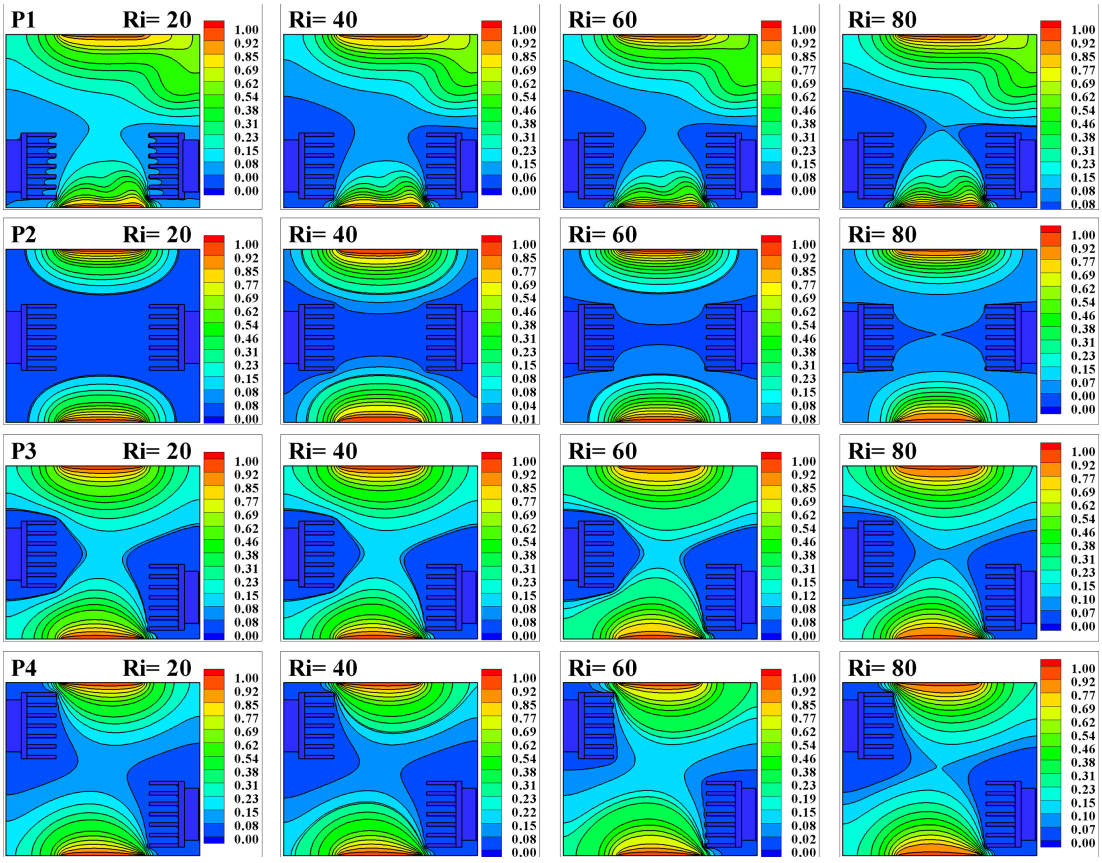

Figure 7: Isotherm contours at various Richardson numbers (*Ri* = 20, 40, 60, 100) for four different saw-tooth fin configurations within the cavity, under fixed conditions of *Re* = 20, *Ha* = 50, and φ = 6%.

Fig. 8 presents the total entropy generation distributions for configurations P1–P4 (corresponding to P1–P4) under varying Ri. At lower *Ri* (*Ri* = 20), entropy generation is primarily localized near the saw-tooth surfaces due to dominant viscous dissipation and thermal gradients. As *Ri* increases, entropy generation becomes more widespread, especially in regions with strong thermal mixing and recirculation. Configurations P1 and P2 exhibit more uniform entropy generation, attributed to symmetrical cooling source placement and consistent thermal boundary layers. In contrast, configurations P3 and P4 show asymmetrical and intensified entropy zones near one of the cooled structures, highlighting the impact of obstacle positioning on thermodynamic irreversibilities. At higher *Ri*, particularly *Ri* = 100, the entropy generation increases significantly near the lower portions of the cavity in P4, emphasizing the role of asymmetric cooling and buoyancy interaction in enhancing local irreversibility. These results suggest that the configuration and positioning of the internal structures substantially affect the entropy generation pattern and thus the thermal performance of the system.

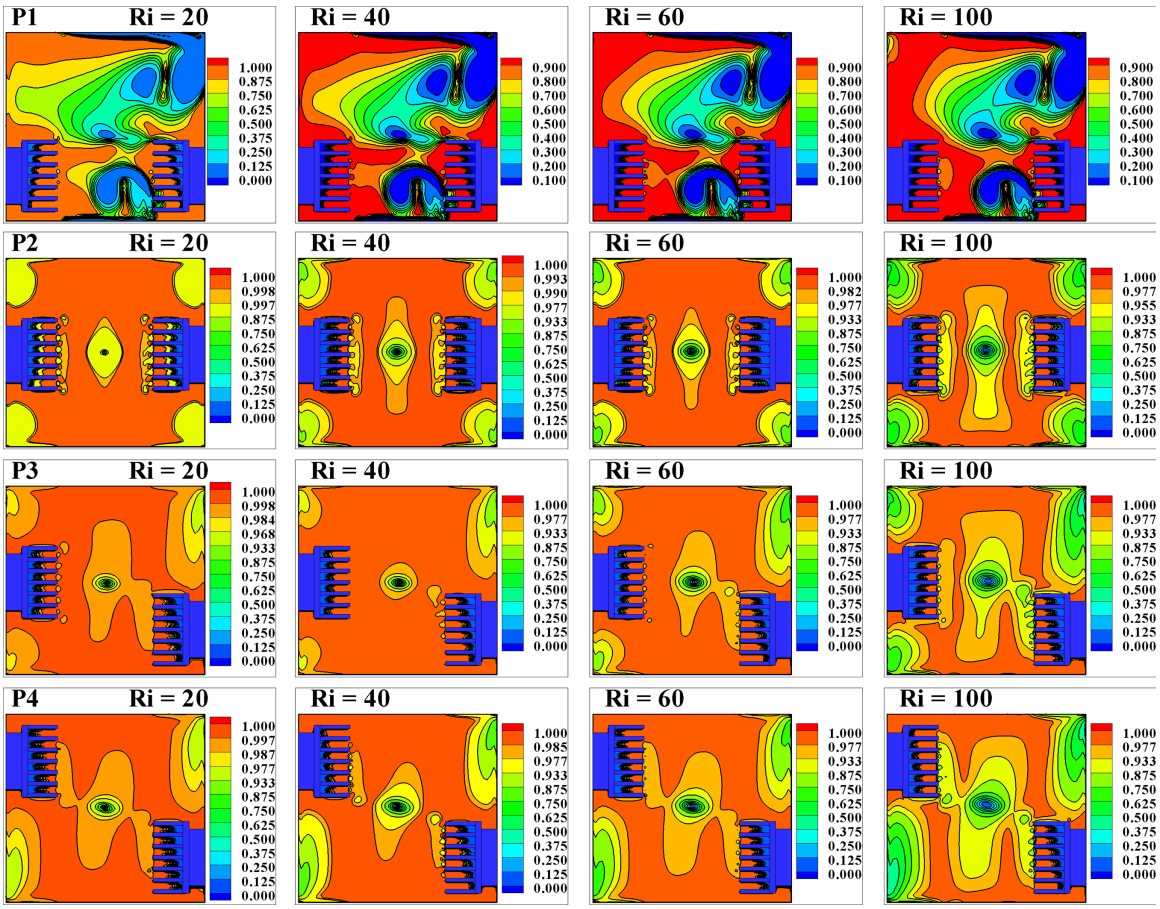

Figure 8: Bejan contours at various Richardson numbers (*Ri* = 20, 40, 60, 100) for four different saw-tooth fin configurations within the cavity, under fixed conditions of *Re* = 20, *Ha* = 50, and φ = 6%.

The influence of increasing nanoparticle volume fraction on the fluid dynamics and thermal behaviour within the cavity is depicted in Figs. 9 and 10. As the volume fraction of the ternary hybrid nanoparticles (MWCNT–Fe_3O_4–Cu) increases, enhancements in thermal conductivity and heat transport are evident across all configurations.

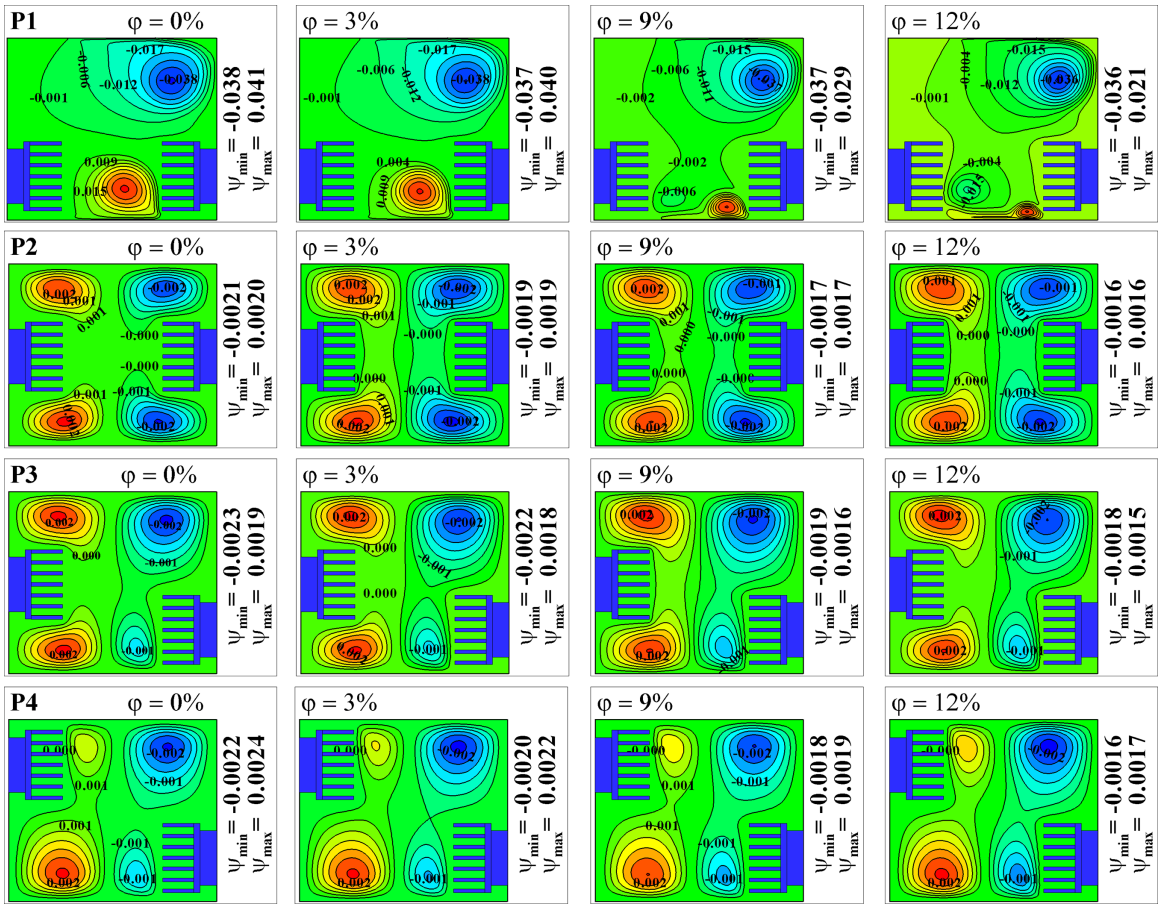

Figure 9: Streamline contours at various nanoparticle volume fraction numbers (φ = 0%, 3%, 9%, 12%) for four different saw-tooth fin configurations within the cavity, under fixed conditions of Ri = 60, Ha = 50, and Re = 20.

In Fig. 9, for φ = 0%, the streamline patterns are dominated by a central circulation cell that conforms to the mixed convection regime governed by the imposed magnetic and buoyancy forces. As φ increases, particularly at φ = 9% and φ = 12%, the vortex structures become more compact and slightly shift toward the cooled saw-tooth surfaces. This tightening of vortical regions is a direct result of increased thermal gradients, which in turn strengthen convective currents due to the elevated heat transfer capacity of the nanofluid. Among the configurations, P2 demonstrates the most symmetric and stable flow enhancement with increasing φ, while P3 and P4 exhibit more pronounced flow distortion due to their asymmetric internal geometry.

Fig. 10 illustrates a significant reduction in thermal boundary layer thickness as φ increases. At φ = 0%, the temperature distribution reveals gradual gradients from the hot to cold regions. However, at φ = 9% and φ = 12%, the isotherms compress toward the cold surfaces and spread more uniformly across the cavity. This behaviour indicates that the ternary nanofluid effectively enhances heat transfer by thinning the thermal boundary layer and increasing thermal conductivity. The isotherms in P2 appear most uniformly distributed at higher φ values, reinforcing the configuration's thermal efficiency due to the symmetric placement of cooling fins. Configurations P3 and P4 again reveal asymmetric thermal fields, where the side closer to the higher-positioned fin exhibits stronger heat extraction.

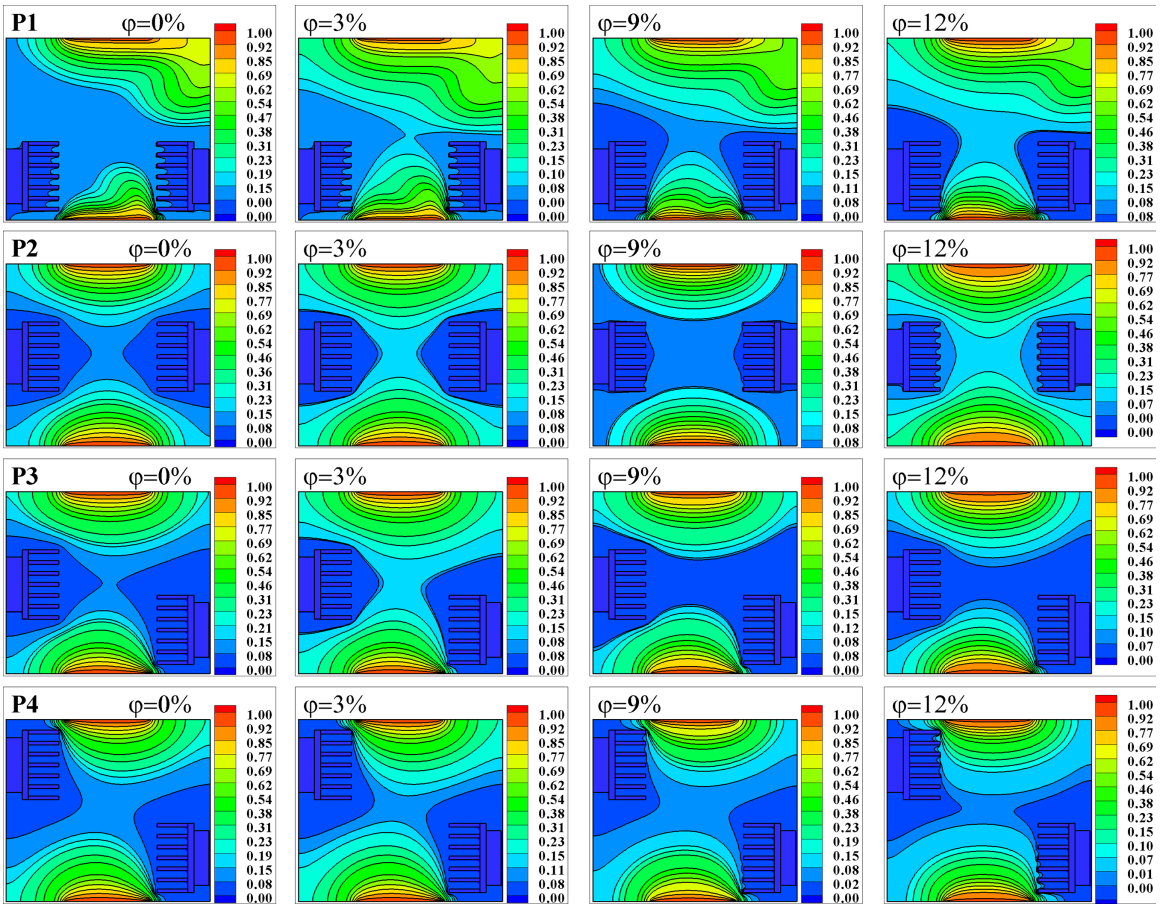

Figure 10: Isotherm contours at various nanoparticle volume fraction numbers (φ = 0%, 3%, 9%, 12%) for four different saw-tooth fin configurations within the cavity, under fixed conditions of Ri = 60, Ha = 50, and Re = 20.

Fig. 11 shows the Bejan number contours for all four configurations as a function of nanoparticle volume fraction. The Bejan number quantifies the relative contribution of thermal irreversibility to total entropy generation. At φ = 0%, the thermal irreversibility is moderate and mostly concentrated near the cold surfaces, consistent with conduction-dominated heat transfer. As φ increases to 9% and 12%, regions of high Bejan number expand and intensify near the cooled fins, showing that thermal gradients dominate over viscous effects. Interestingly, the transition in entropy behaviour across configurations varies. Configuration P2 consistently shows more distributed and moderate Bejan values, suggesting a balance between heat and fluid friction irreversibilities. In contrast, P4 demonstrates sharper, more localized peaks in the Bejan number with increasing φ, reflecting heightened thermal irreversibility due to geometric asymmetry and intensified thermal transport.

Fig. 12 illustrates the kinetic energy contours for four different saw-tooth fin configurations (P1–P4) under the fixed parameters of Ri = 100, Re = 80, Ha = 0, and φ = 0%. These contours represent the distribution of kinetic energy throughout the cavity and provide insight into the intensity and localization of fluid motion driven by mixed convection. In configuration P1, the kinetic energy is concentrated near the center-top of the cavity, with relatively weak motion throughout the domain. This suggests a less vigorous circulation pattern due to the symmetrical positioning of the saw-tooth structures at lower vertical positions along the sidewalls, which inhibits strong buoyancy-driven vortex development. Configuration P2, where both fins are placed at mid-height (0.5 L), shows significantly enhanced kinetic energy zones on both sides of the

cavity. This central placement disrupts the vertical flow paths more effectively, leading to intensified vortex formation and greater momentum transfer within the fluid. In P3, with asymmetric placement (left fin at mid-height and right fin at 0.25L), the kinetic energy is notably higher near the centrally positioned structure, and slightly weaker near the lower fin. This indicates an asymmetric circulation pattern with stronger convective currents in the upper half of the domain. Lastly, in P4, where one fin is near the top (0.75L) and the other at 0.25 L, it exhibits the most uniform and intense kinetic energy distribution. This configuration encourages full-domain circulation, activating both upper and lower regions of the cavity, and demonstrates the most efficient fluid mixing. The enhanced kinetic energy in P4 highlights the potential of vertically distributed fins to stimulate robust flow dynamics and optimize heat removal.

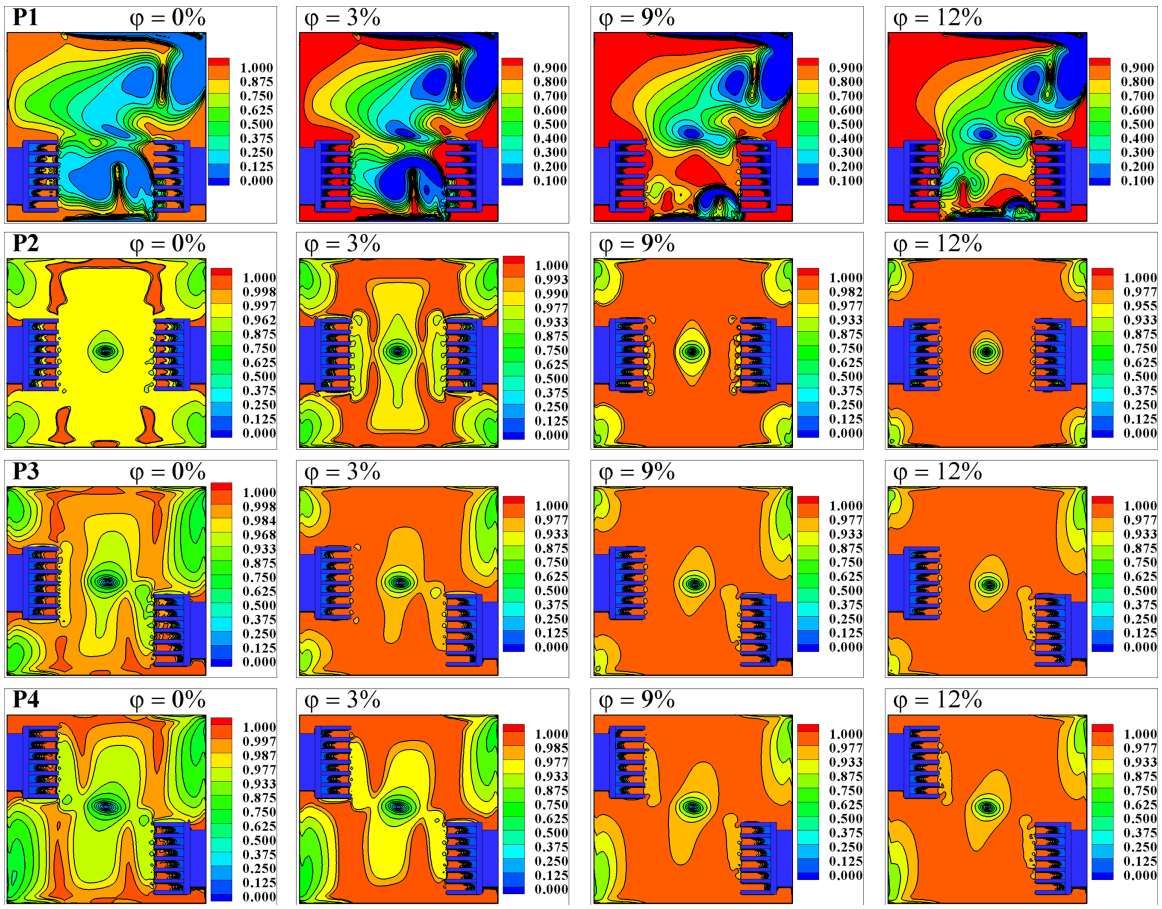

Figure 11: Bejan contours at various nanoparticle volume fraction numbers (φ = 0%, 3%, 9%, 12%) for four different saw-tooth fin configurations within the cavity, under fixed conditions of Ri = 60, Ha = 50, Re = 20.

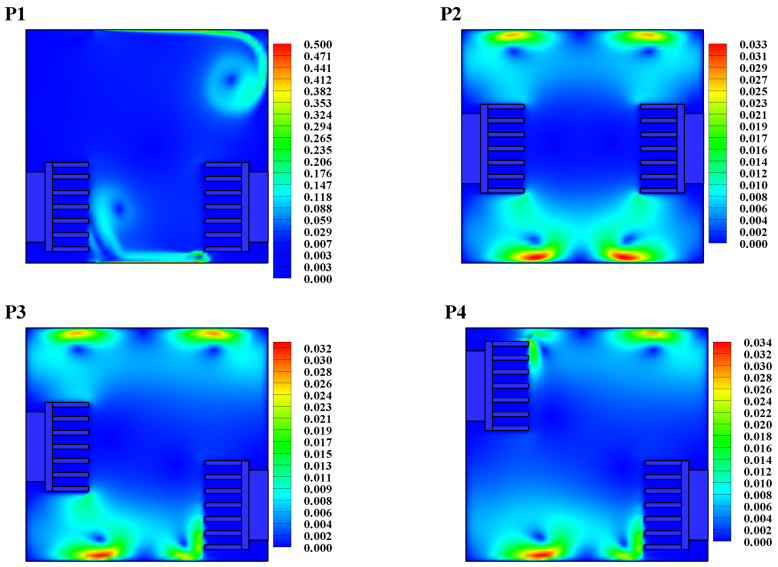

Figure 12: Kinetic Energy contours for four different saw-tooth fin configurations within the cavity, under fixed conditions of Ri = 100, Ha = 0, Re = 80 and φ = 0%.

Fig. 13 presents velocity contours along the horizontal direction (x-axis) at the mid-plane (y = 0.5L) for Richardson numbers Ri = 20, 40, 60, and 100 across the four configurations P1–P4, with Re = 80, Ha = 0, and φ = 0%. These profiles provide a clearer depiction of the influence of Richardson number on horizontal flow velocity. In P1, the velocity profiles display modest peaks and fluctuations across all Ri values, indicating limited fluid acceleration. The symmetrical low-positioned fins in this configuration create a more stagnant flow zone at the mid-height, with weaker momentum transfer. On the other hand, P2 exhibits more pronounced velocity peaks, particularly at low Ri (20 and 40), reflecting enhanced forced convection effects due to better fin-induced obstruction and channelling at the central height. As Ri increases, the curves flatten slightly, but the velocity remains higher than in P1. In P3, the asymmetry of fin placement leads to uneven velocity distribution across the domain. The velocity peaks are shifted laterally, reflecting non-uniform flow acceleration. At moderate Ri (40 and 60), P3 shows effective interaction between buoyancy and forced convection, though not as optimized as P4. Lastly, P4 consistently shows the highest peak velocities, especially at low and moderate Ri values. The staggered fin positioning promotes effective flow redirection and momentum amplification across the cavity. As Ri increases to 100, buoyancy dominates and reduces the velocity gradients, yet P4 maintains superior flow strength due to its spatial fin distribution that activates a broader convective pathway.

4.2 Quantitative Assessment of Heat Transfer and Entropy Generation Characteristics

The influence of Hartmann number on average Nusselt number can be visualized through Fig. 14 which illustrates the variations of the average Nusselt number along the north wall of the enclosure vs. Richardson number (Ri) for different Hartmann numbers (Ha = 0, 50, 100, 150) across the four saw-tooth fin configurations (P1–P4), with fixed Re = 60 and φ = 6%. Across all configurations, we can see an increase in the Hartmann number results in a decrease in convective heat transfer at lower Ri, due to the suppression of velocity fields by the magnetic damping (Lorentz force). Moreover, as the Richardson number increases, the buoyancy effects dominate, enhancing heat transfer despite stronger magnetic fields. This is especially noticeable for Ri = 100, where the average Nusselt number increases significantly for all configurations, even at higher Ha. Among the configurations, P2 consistently records the highest $\overline{Nu}_{East}$ values, confirming its

superior thermal performance due to symmetric placement of the cooled structures. On the other hand, configurations P3 and P4 exhibit lower performance, highlighting the thermal penalty of asymmetrical internal obstructions under magnetic effects.

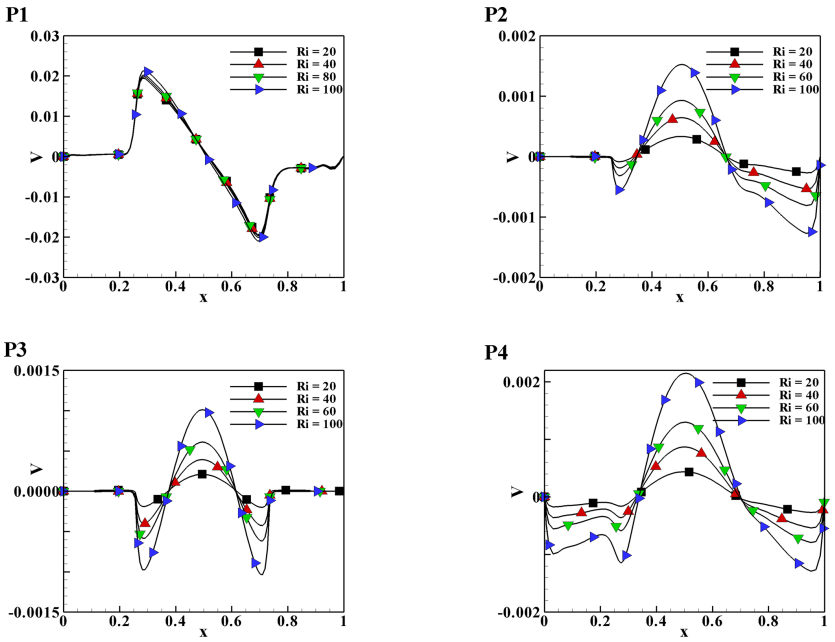

Figure 13: Velocity contours vs. x at various Richardson numbers (*Ri* = 20, 40, 60, 100) for four different saw-tooth configurations within the cavity, under fixed conditions of *Re* = 80, *Ha* = 0, and φ = 0%.

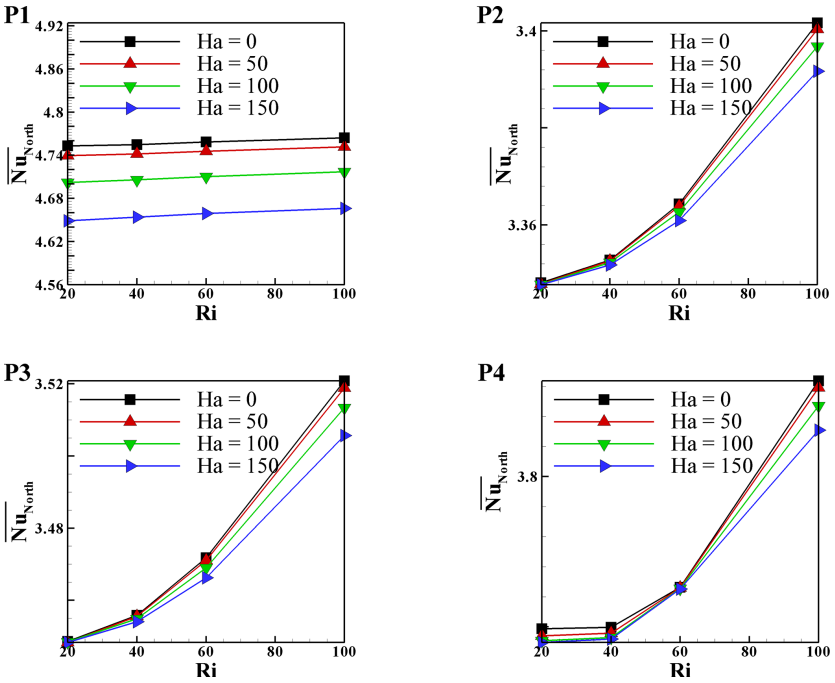

Figure 14: Variations of average Nusselt number vs. Richardson number for different Hartmann numbers (*Ha* = 0, 50, 100, 150) for four different saw-tooth fin configurations within the cavity, for *Re* = 60, φ = 6%.

The influence of nanoparticle volume fraction on average Nusselt Number can be visualized through Fig. 15 which presents the effect of varying nanoparticle volume fraction (φ = 3%, 6%, 9%, 12%) on the average Nusselt number for the same four configurations, with fixed *Re* = 60 and *Ha* = 50. It can be seen that the average Nusselt number increases marginally with rising φ in all configurations, demonstrating that ternary nanofluid enhances heat transfer through improved thermal conductivity and augmented thermal gradients. The improvement is more prominent at higher Richardson numbers, where buoyancy-induced convection amplifies the influence of enhanced thermal conductivity. Again, P2 displays the most substantial increase in heat transfer with φ, whereas P3 and P4 show minimal variation, confirming that the spatial distribution of the fins significantly governs the thermal utilization of nanoparticles.

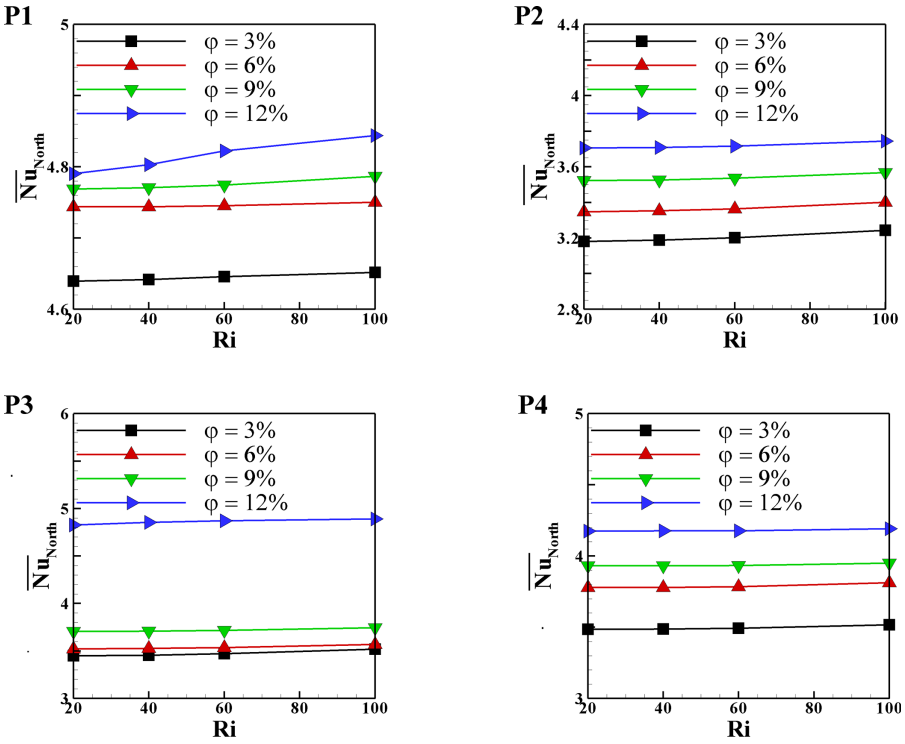

Figure 15: Variations of average Nusselt number vs. Richardson number for different nanoparticle volume fractions (φ = 3%, 6%, 9%, 12%) for four different saw-tooth fin configurations within the cavity, for *Re* = 60, *Ha* = 50.

The influence of Reynolds number on average Nusselt number can be visualized in Fig. 16 which explores the variation of $\overline{Nu}_{North}$ with Richardson numbers for different Reynolds numbers (*Re* = 20, 40, 60, 80), under constant *Ha* = 50 and φ = 12%. We can see at low Richardson numbers (*Ri* = 20), forced convection dominates, and the Nusselt number increases significantly with higher Reynolds numbers, due to increased flow inertia. However, at high Richardson numbers (*Ri* = 100), natural convection becomes dominant, and the influence of Re is diminished, resulting in converging trends of Nusselt number across all Re values. This indicates a transition from forced to natural convection regimes, especially evident in symmetric configurations (P1 and P2). P3 and P4, which have asymmetrical obstacle placements, show reduced sensitivity to Reynolds number due to disrupted flow development and uneven circulation paths. A summary of parametric influence on thermal performance is listed in Table 5.

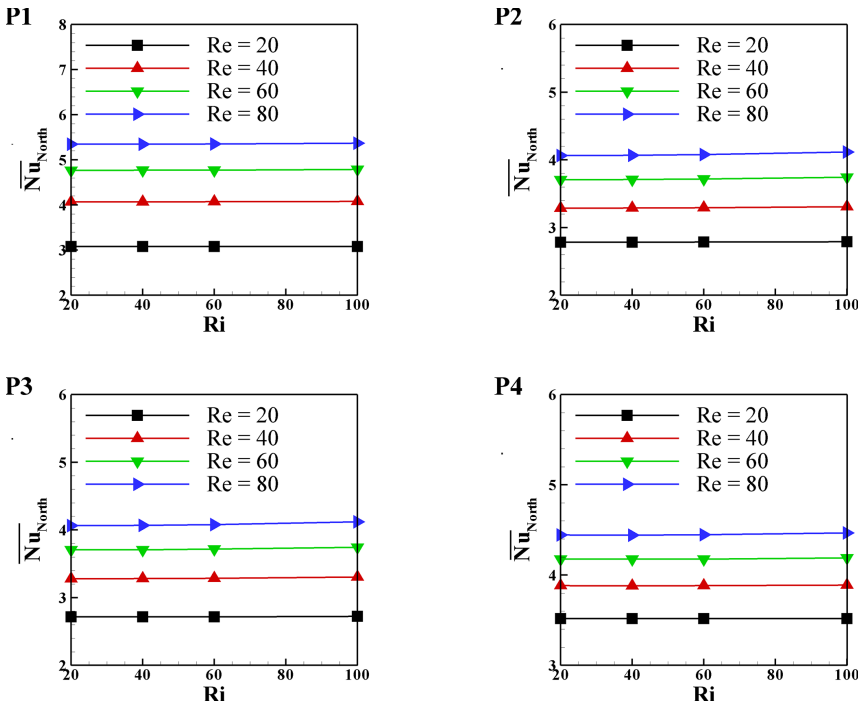

Figure 16: Variations of average Nusselt number vs. Richardson number for different Reynolds numbers (*Re* = 20, 40, 60, 80) for four different saw-tooth fin configurations within the cavity, for *Ha* = 50, φ = 12%.

Table 5: Summary of parametric influence on thermal performance.

Parameter	Primary Impact	Most Effective Configuration
Hartmann number	Suppresses flow and reduces heat transfer at low *Ri*; buoyancy dominates at high Ri	P2
Nanoparticle volume fraction (φ)	Enhances $\overline{Nu}_{East}$ moderately, especially at high *Ri*	P2
Reynolds number	Increases $\overline{Nu}_{East}$ significantly under forced convection regime (low *Ri*)	P1 and P2

This section explores the influence of key dimensionless parameters Hartmann number (*Ha*), nanoparticle volume fraction (φ), and Reynolds number (*Re*) on the total entropy generation within a square cavity filled with a MWCNT–Fe_3O_4–Cu/water ternary hybrid nanofluid. The cavity contains variable-position saw-tooth internal structures serving as localized cooling elements. Variations are analysed across four distinct saw-tooth configurations (P1 to P4) described in the physical model.

The effect of Hartmann number can be visualized through Fig. 17 which presents the variation of total entropy generation S_T with Richardson number (Ri) for different Hartmann numbers (*Ha* = 0, 50, 100, 150), at a fixed Reynolds number of *Re* = 60 and nanoparticle concentration φ = 6%. Across all configurations (P1–P4), an increasing trend of entropy generation is observed with increasing Ri, which is expected due to the enhanced natural convection contribution. The influence of the magnetic field is more pronounced at higher *Ri*. At lower *Ri* (dominated by forced convection), the Lorentz force has a subdued impact. However, as *Ri* increases, the suppression of fluid motion by the magnetic field becomes more effective, causing noticeable

changes in entropy production. Among the configurations, P4 exhibits the highest entropy generation across all Ha values, indicating that positioning the top saw-tooth structure higher (at 0.75*L*) increases flow disturbances and thermal gradients.

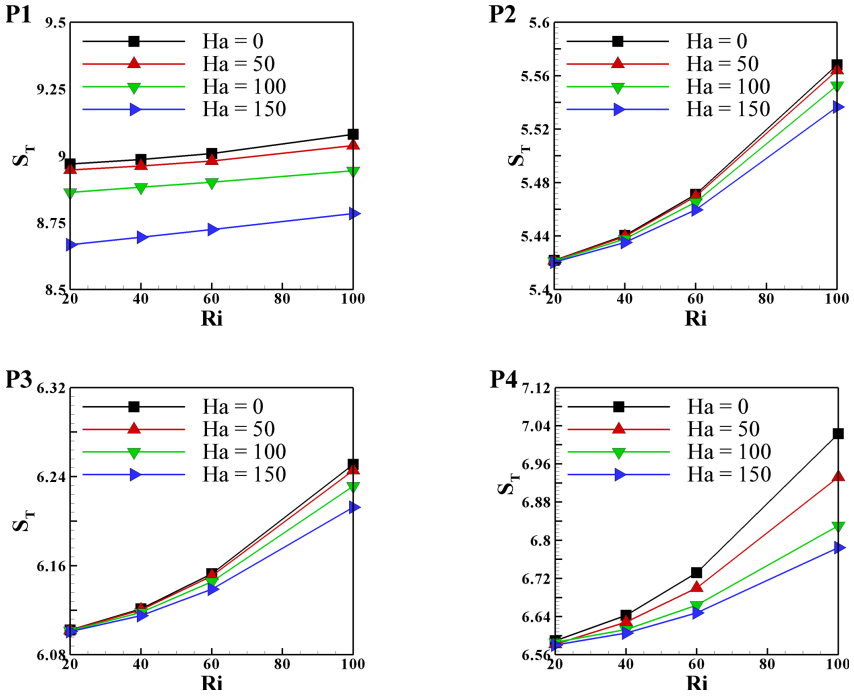

Figure 17: Variations of total entropy generation vs. Richardson number for different Hartmann numbers (*Ha* = 0, 50, 100, 150) for four different saw-tooth fin configurations within the cavity, for *Re* = 60, φ = 6%.

The effect of nanoparticle volume fraction can be visualized through Fig. 18, which demonstrates the impact of varying nanoparticle volume fractions (φ = 3%, 6%, 9%, 12%) on the total entropy generation with *Ri*, for *Ha* = 50 and *Re* = 60. The trends show a monotonic increase in entropy generation with both increasing φ and *Ri*. This behaviour is attributed to the improved thermal conductivity of the fluid with higher nanoparticle content, which enhances convective heat transfer but also raises irreversibilities. Configuration P4 again registers the highest entropy values, suggesting that the staggered and non-symmetric placement of saw-tooth structures causes greater local temperature gradients, increasing thermal irreversibilities. The minimal entropy values are observed for P1, which maintains a symmetric internal structure positioning, promoting more uniform flow and heat distribution.

The effect of Reynolds number can be visualized through Fig. 19, which illustrates the variation of total entropy generation vs. Ri for different Reynolds numbers (*Re* = 20, 40, 60, 80) at a fixed φ = 12% and *Ha* = 50. Here, entropy generation remains relatively constant for each configuration as Ri increases. This indicates that under strong forced convection conditions (higher Re), the impact of buoyancy (and thus *Ri*) on entropy generation diminishes. Forced convection dominates the thermal transport mechanism, minimizing the contribution of natural convection. Notably, P1 again yields the lowest entropy levels, reinforcing the efficiency of symmetrical saw-tooth positioning in minimizing entropy generation. Meanwhile, the performance gap between configurations widens as Re increases, highlighting the importance of internal structure placement in managing convective flow regimes. A summary of heat transfer enhancement rates at different Richardson numbers for the different considered positions of the inner saw-tooth structures are presented in Table 6.

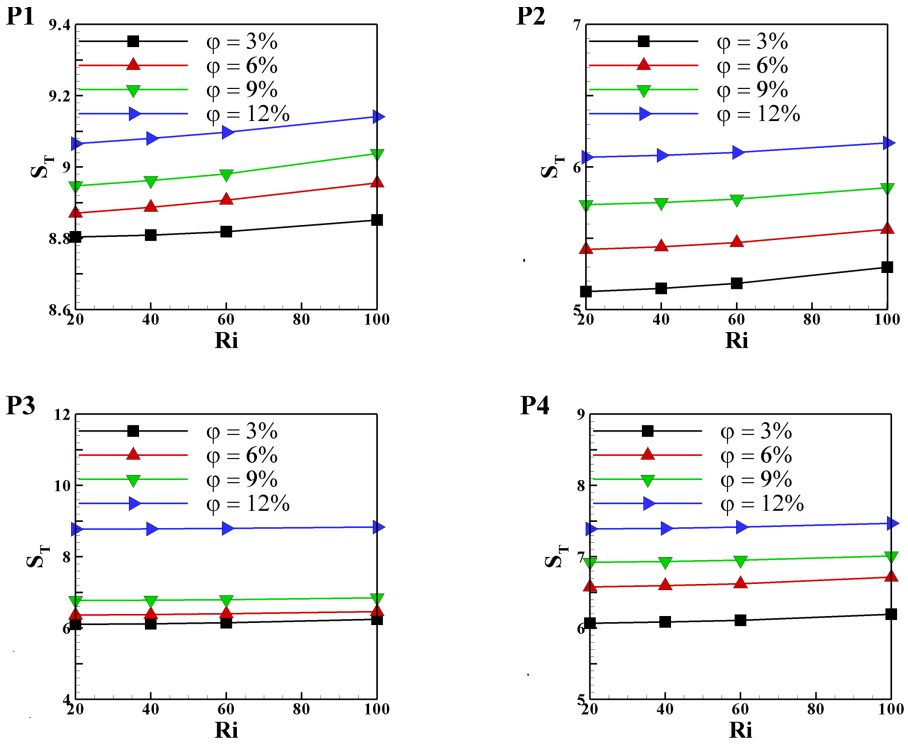

Figure 18: Variations of total entropy generation vs. Richardson number for different nanoparticle volume fractions (φ = 3%, 6%, 9%, 12%) for four different saw-tooth configurations within the cavity, for *Re* = 60, *Ha* = 50.

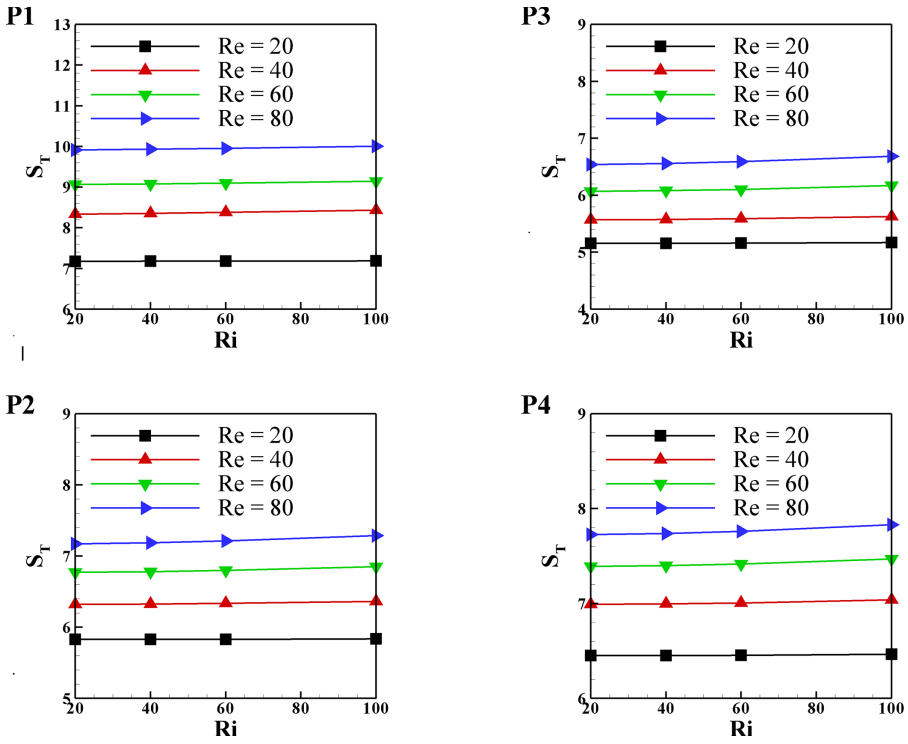

Figure 19: Variations of total entropy generation vs. Richardson number for different Reynolds numbers (*Re* = 20, 40, 60, 80) for four different saw-tooth fin configurations within the cavity, for φ = 12%, *Ha* = 50.

Table 6: Summary of heat transfer enhancements at different Richardson numbers for the different considered positions of the inner saw-tooth structures.

Ri	**20**	**40**	**60**	**80**
φ = 3%	2.734	3.228	3.524	3.762
φ = 6%	4.109	4.842	5.523	5.886
φ = 9%	3.869	4.842	5.016	5.415
φ = 12%	2.547	2.998	3.185	3.401
P1 at (Ha = 50, Re = 80)				
Ri	20	40	60	80
φ = 3%	5.09898	4.991034	4.869359	4.545455
φ = 6%	10.43791	10.25105	10.00594	9.382284
φ = 9%	16.0168	15.78004	15.40974	14.51049
φ = 12%	21.89562	21.578	21.11045	19.93007
P2 at (Ha = 50, Re = 80)				
Ri	20	40	60	80
φ = 3%	5.09898	5.020921	4.867913	4.541485
φ = 6%	13.91722	13.80753	13.6539	13.30422
φ = 9%	16.04679	21.578	21.10419	19.91266
φ = 12%	21.89562	63.5696	63.69843	61.07715
P3 at (Ha = 50, Re = 80)				
Ri	20	40	60	80
φ = 3%	5.867	14.647	18.225	23.858
φ = 6%	5.916	14.700	18.250	23.912
φ = 9%	6.170	14.979	18.369	23.960
φ = 12%	7.115	15.998	19.036	24.508
P4 at (Ha = 50, Re = 80)				

To estimate the enhancement of heat transfer between the case of (φ = 3%, 6%, 9% and 12%) and the pure fluid (base fluid) case, the enhancement is defined as:

$$En_{\overline{Nu}} = \frac{\overline{Nu}\,(\varphi = 3\%, 6\%, 9\%, 12\%)}{\overline{Nu}\,(base\,fluid)} \times 100 \tag{23}$$

Table 6 presents the heat transfer enhancements at different Richardson numbers for the different considered positions of the inner saw-tooth structures at Ha = 50 and Re = 80. For position P1, the maximum eat transfer is 5.886 at φ = 6%, Ri = 80, showing best performance here. Moreover, 6% volume fraction is optimal; beyond that (φ = 9%, 12%) the performance slightly decreases, likely due to increased viscosity. On the other hand, the heat transfer increases with Ri (stronger natural convection), but φ = 12% shows a negative impact. For the Position P2, $\overline{Nu}_{East}$ decreases with Ri (opposite trend), suggesting that forced convection dominates in this case. Thus, the heat transfer consistently improves with φ, peaking at φ = 12% and Ri = 20 and the best case is obtained for φ = 12%, Ri = 20 where $\overline{Nu}_{North}$ = 21.896. For the position P3, extremely high values are obtained at φ = 12%, Ri = 40–80, with peak $\overline{Nu}_{East}$ = 63.698, suggest P3 is thermally dominant. This

configuration benefits greatly from higher φ and moderate to high Ri and shows nonlinear enhancement in $\overline{Nu}_{North}$ as φ and Ri increase. Thus, optimal case overall is P3, φ = 12%, Ri = 60 or 80. For the position P4, Steady increase in $\overline{Nu}_{North}$ with both φ and Ri. Peak value is 24.508 at φ = 12%, Ri = 80. Thus, P4 is nearly as effective as P3 in some cases but less extreme in trend.

Fig. 20 presents histograms of average Nusselt numbers along the north wall of the cavity vs. Richardson number (Ri) for various nanoparticle volume fractions (φ = 3%, 6%, 9%, 12%), at fixed conditions Re = 80 and Ha = 50. Fig. 20 provides insight into the heat transfer performance of the four saw-tooth fin configurations (P1–P4) by examining the average Nusselt number $\overline{Nu}_{North}$ on the cavity's east wall. The analysis considers the combined effects of nanoparticle concentration and Richardson number under mixed convection conditions (Re = 80, Ha = 50). Regarding the effect of nanoparticle volume fraction (φ), across all configurations, the average Nusselt number consistently increases with increasing φ, indicating enhanced thermal conductivity due to the addition of more nanoparticles. The highest heat transfer rates are observed at φ = 12%, highlighting the effective role of ternary hybrid nanofluids in boosting convective heat transport. On the other hand, for the effect of Richardson number (Ri); for each configuration, $\overline{Nu}_{North}$ also shows a positive correlation with Ri, though the rate of increase is relatively modest. This reflects the growing contribution of buoyancy forces to the mixed convection regime as Ri rises, slightly improving heat transfer on the vertical wall. A configuration-wise comparison shows the following:

- P1 (symmetric placement at 0.25L), shows a moderate but consistent rise in $\overline{Nu}_{North}$. The Nusselt number at φ = 12% and Ri = 100 is approximately 5.533.
- P2 (symmetric placement at 0.5L), displays the lowest heat transfer rates among all configurations, with $\overline{Nu}_{North}$ reaching only 4.106 at φ = 12% and Ri = 100. This suggests that placing both structures at mid-height may restrict vertical thermal circulation.
- P3 (asymmetric: 0.25 and 0.5L), offers improved performance over P2, reaching a $\overline{Nu}_{North}$ of 5.533 at φ = 12% and Ri = 100 on par with P1. The slightly higher performance reflects the benefit of vertical asymmetry.
- P4 (asymmetric: 0.25 and 0.75L), yields the highest Nusselt numbers overall, with a peak value of 5.601 at φ = 12% and Ri = 100. This configuration facilitates stronger thermal gradients and promotes mixing by disrupting the thermal boundary layer more effectively.

Thus, the optimal heat transfer conditions occur under the following conditions; configuration P4 (cooling structures at 0.25 and 0.75L), nanoparticle volume fraction φ = 12%, Richardson number Ri = 100, Re = 80 and Ha = 50. Under these conditions, the average Nusselt number peaks at 5.601, indicating the most efficient thermal performance within the tested parameter intervals.

Fig. 21 presents histograms of total entropy generation as a function of Richardson number (Ri = 20, 40, 60, 100) for four saw-tooth fin configurations (P1–P4) at Re = 80 and Ha = 50, with varying nanoparticle volume fractions (φ = 3%, 6%, 9%, and 12%). The entropy generation trends offer critical insights into how buoyancy–inertia interplay (represented by the Richardson number) and nanofluid concentration affect thermodynamic irreversibility in each configuration. For instance, P1 consistently yields the highest total entropy generation values across all Ri and φ. This is attributed to the symmetric positioning of the fins near the bottom, which intensifies thermal gradients and viscous dissipation due to high recirculation near the walls. Moreover, the entropy generation increases with both Ri and φ, indicating that stronger buoyancy and higher nanoparticle loading contribute to increased thermal and viscous irreversibility. Thus, the maximum value is 10.1 at Ri = 100 and φ = 12%. On the other hand, P2 exhibits the lowest entropy generation levels, particularly at lower Ri values. Actually, the mid-height placement of fins stabilizes the flow and results in more uniform heat distribution, thereby reducing irreversibility. Increasing ϕ leads to slight increases in entropy generation, though the effect is less pronounced compared to P1. Thus, minimum observed value is

5.46 at Ri = 20 and φ = 3%. P3 demonstrates a moderate entropy generation profile, higher than P2 but lower than P1 as the asymmetric positioning (0.5 and 0.25L) introduces partial disruption of the flow symmetry, increasing convective mixing without fully intensifying viscous losses. P4 also shows a moderate to high entropy generation trend, closely resembling P3 but slightly higher values at higher Ri as the placement at 0.75L and 0.25L enhances complex flow paths and promotes localized velocity gradients, particularly at high Ri.

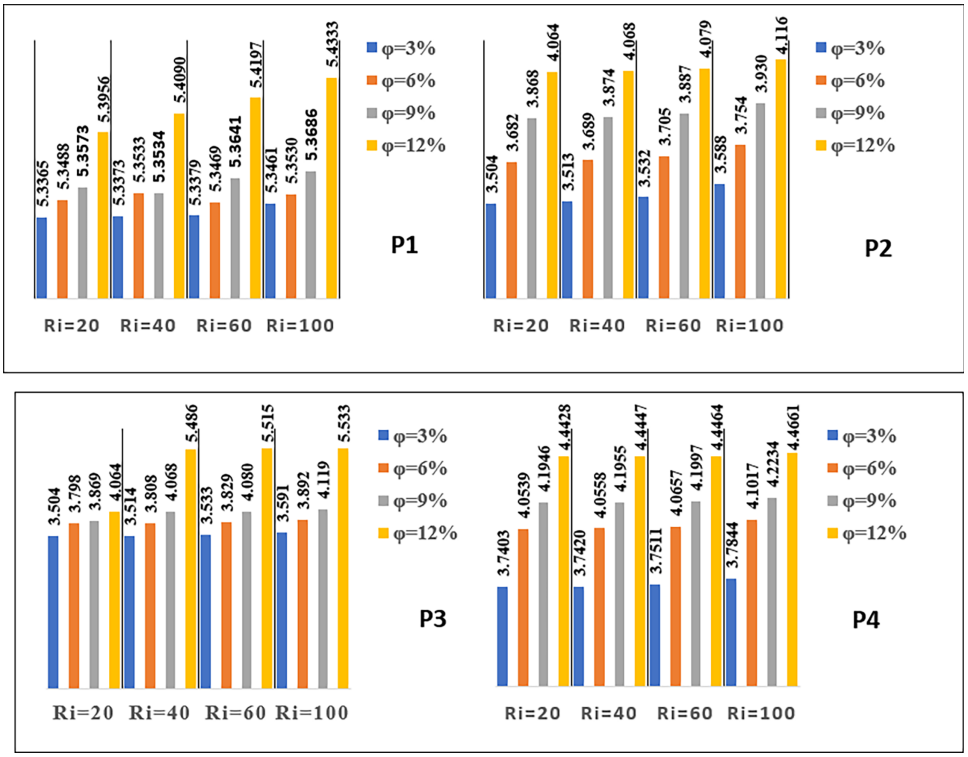

Figure 20: Histograms of average Nusselt numbers along the east wall of the enclosure vs. Richardson numbers *at* different nanoparticle volume fractions for four different saw-tooth fin configurations within the cavity at Re = 80 and Ha = 50.

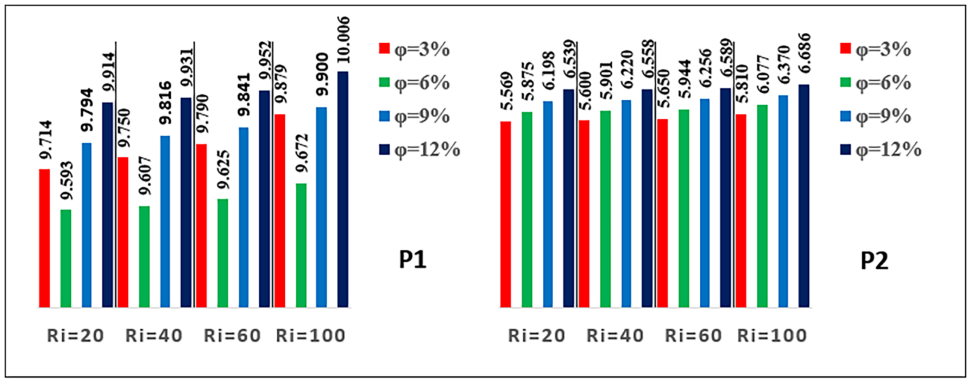

Figure 21: (Continued)

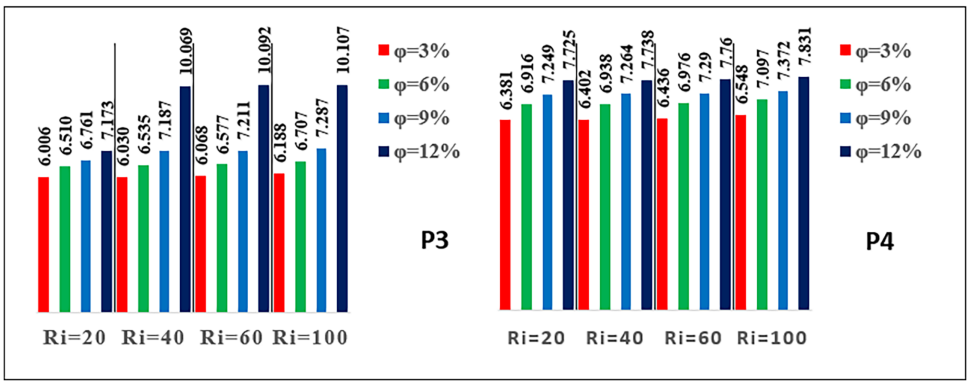

Figure 21: Histograms of total entropy generation vs. Richardson numbers at different nanoparticle volume fractions for four different saw-tooth fin configurations within the cavity at *Re* = 80 and *Ha* = 50.

5 Conclusions and Future Directions

This study numerically investigated the thermofluidic behaviour and entropy generation characteristics of magnetohydrodynamic (MHD) mixed convection in a square cavity filled with a ternary hybrid nanofluid (MWCNT–Cu–Fe_3O_4/water). The system incorporated two internally cooled saw-tooth fins arranged in four vertical configurations (P1–P4) and was subjected to an inclined magnetic field. The impacts of key dimensionless parameters, namely Reynolds number (Re), Richardson number (Ri), Hartmann number (Ha), and nanoparticle volume fraction (φ), were systematically analysed.

The results demonstrate that nanoparticle loading significantly enhances heat transfer performance up to an optimal range ($\varphi \approx$ 6%–9%), beyond which the increasing viscosity and flow resistance reduce the thermal benefits. The highest thermal performance was achieved at φ = 12% in configurations P3 and P4, where convective mixing is most effective. In addition, heat transfer was found to improve with increasing Richardson number, particularly in configurations where buoyancy forces strengthen thermal circulation, such as P1 and P4. However, this enhancement is accompanied by increased entropy generation due to intensified thermal gradients and flow disturbances.

The influence of the magnetic field, represented by the Hartmann number, revealed that increasing Ha suppresses convective motion due to the Lorentz force, leading to reduced heat transfer at lower *Ri*. Entropy generation initially increases at moderate *Ha* due to magnetic effects but tends to stabilize or slightly decrease at higher values as the flow becomes increasingly damped.

From a configuration perspective, P3 exhibited the best overall thermal performance, achieving the highest average Nusselt numbers due to enhanced flow disruption and mixing. P4 also demonstrated strong performance, especially at higher Ri, owing to its complex flow structures. In contrast, P1 showed moderate heat transfer but relatively high entropy generation, indicating lower thermodynamic efficiency, while P2 yielded the lowest heat transfer alongside minimal entropy generation, making it suitable for applications prioritizing reduced irreversibility.

Entropy analysis further confirmed that P1 produces the highest total entropy generation due to intensified viscous and thermal effects, whereas P2 consistently minimizes entropy generation under most conditions. Configurations P3 and P4 provide a balanced compromise between enhanced heat transfer and acceptable entropy levels, highlighting their suitability for high-efficiency thermal systems. Overall, entropy generation increases with both nanoparticle concentration and Richardson number, reflecting the trade-off between improved thermal conductivity and increased irreversibility.

Despite these promising findings, several challenges were encountered. The incorporation of ternary hybrid nanofluids introduces strong nonlinearities in the governing equations, significantly increasing computational complexity, particularly at high Reynolds and Hartmann numbers. Moreover, accurately resolving sharp gradients near the saw-tooth fins required highly refined meshes, leading to increased computational cost and memory demand. At higher nanoparticle concentrations (e.g., φ = 12%), stability issues were also observed due to elevated viscosity and associated flow resistance.

Future research can build upon this work by extending the present two-dimensional model to three-dimensional configurations, which would provide a more realistic representation of practical thermal systems and reveal additional flow features. Furthermore, investigating transient behaviour under time-dependent conditions, such as fluctuating magnetic fields or pulsed heat sources, would offer deeper insight into the dynamic evolution of the flow and thermal fields.

In summary, this study highlights the importance of optimizing fin configuration, nanoparticle concentration, and magnetic field strength to achieve an effective balance between heat transfer enhancement and entropy generation. Among the investigated cases, configuration P3 emerges as the most thermally efficient, while P2 is preferable for applications requiring minimal irreversibility, offering valuable design guidance for advanced MHD-based thermal management systems employing hybrid nanofluids.

Acknowledgement: None.

Funding Statement: This work was supported by the Deanship of Scientific Research, Vice Presidency for Graduate Studies and Scientific Research, King Faisal University, Saudi Arabia (Grant No. 253931).

Availability of Data and Materials: Data sets generated during the current study are available from the corresponding author on reasonable request.

Ethics Approval: Not applicable.

Conflicts of Interest: The author declares no conflicts of interest.

Nomenclature

Latin Symbols

B	Magnetic field intensity
Cp	Specific heat capacity (J/kg·K)
g	Gravitational acceleration (m/s^2)
k	Thermal conductivity (W/m·K)
L	Characteristic length of the square cavity (m)
Ha	Hartmann number
$\overline{Nu}$	Average Nusselt number
n	Normal direction
Pr	Prandtl number
P	Reference pressure scale
q	Heat flux vector (W/m^2)
Re	Reynolds number
Ri	Richardson number
$S^\star$	Dimensionless entropy generation per unit volume (W/m^3·K)
Tc	Cold wall temperature (K)
Th	Hot wall temperature (K)
T	Temperature (K)
(U,V)	Dimensionless velocity components

(X,Y)	Dimensionless Cartesian coordinates

Greek Symbols

φ	Nanoparticle volume fraction
α	Thermal diffusivity (m^2/s)
θ	Dimensionless temperature
ν	Kinematic viscosity (m^2/s)
μ	Dynamic viscosity (kg/(m·s))
ρ	Fluid density (kg/m^3)
β	Thermal expansion coefficient (K^{-1})
Ψ	Irreversibility coefficient
Ω	Global domain
σ	Effective electrical conductivity (μS/cm)

Subscripts

c	Cold
h	Hot
loc	Local
tot	Total

References

1. Benabdallah F, Ghachem K, Hassen W, Baya H, Albalawi H, Kolsi L. MHD convective flow of CNT/water-nanofluid in a 3D cavity incorporating hot cross-shaped obstacle. Comput Model Eng Sci. 2025;145(2):1839–61. doi:10.32604/cmes.2025.071678.
2. Souayeh B. Numerical analysis of magnetohydrodynamics mixed convection and entropy generation in a double lid-driven cavity using ternary hybrid nanofluids. Adv Theory Simul. 2025;8(5):2401357. doi:10.1002/adts.202401357.
3. Souayeh B. Influence of boundary condition variations on magnetohydrodynamics natural convection and entropy generation in a ternary nanofluid filled-square cavity with elliptic cylinder. Phys Fluids. 2025;37(4):042009. doi:10.1063/5.0269514.
4. Shateri A, Ganji AM, Jalili P, Jalili B, Ganji DD. Utilizing Python for numerical analysis of bioconvection in magnetized Casson-Maxwell nanofluid systems with gyrotactic microorganisms: an investigation of dominant factors. Results Eng. 2025;25(12):103760. doi:10.1016/j.rineng.2024.103760.
5. Hajizadeh S, Jalili P, Jalili B, Alam MM, Ali MR, Hendy AS, et al. Innovative binary nanofluid approach with copper (Cu-EO) and Magnetite (Fe_3O_4–EO) for enhanced thermal performance. Case Stud Therm Eng. 2024;63(3):105191. doi:10.1016/j.csite.2024.105191.
6. Qureshi MA, Hussain S, Sadiq MA. Numerical simulations of MHD mixed convection of hybrid nanofluid flow in a horizontal channel with cavity: impact on heat transfer and hydrodynamic forces. Case Stud Therm Eng. 2021;27:101321. doi:10.1016/j.csite.2021.101321.
7. Ahmed SE, Raizah ZAS. Magnetic mixed convection of a Casson hybrid nanofluid due to split lid driven heat generated porous triangular containers with elliptic obstacles. J Magn Magn Mater. 2022;559(4):169549. doi:10.1016/j.jmmm.2022.169549.
8. Armaghani T, Sadeghi MS, Rashad AM, Mansour MA, Chamkha AJ, Dogonchi AS, et al. MHD mixed convection of localized heat source/sink in an Al_2O_3-Cu/water hybrid nanofluid in L-shaped cavity. Alex Eng J. 2021;60(3):2947–62. doi:10.1016/j.aej.2021.01.031.
9. Rajarathinam M, Akermi M, Khan MI, Nithyadevi N. MHD mixed convection heat transfer of copper water nanofluid in an inclined porous cavity having isothermal solid block. J Magn Magn Mater. 2024;593:171845. doi:10.1016/j.jmmm.2024.171845.

10. Ahmed SE, Raizah Z, Arafa AAM, Hussein SA. FEM treatments for MHD highly mixed convection flow within partially heated double-lid driven odd-shaped enclosures using ternary composition nanofluids. Int Commun Heat Mass Transf. 2023;145:106854. doi:10.1016/j.icheatmasstransfer.2023.106854.
11. Alqurashi MS, Bayones FS, Abo-Dahab SM, Abd-Alla AM, Soliman MS. Mixed convection effect on MHD Oldroyd-B nanofluid flow over a stretching sheet through a porous medium with viscous dissipation-chemical engineering applications. Alex Eng J. 2025;125:507–25. doi:10.1016/j.aej.2025.04.056.
12. Das P, Mamun MAH. Predicting MHD mixed convection in a semicircular cavity with hybrid nanofluids using AI. Heliyon. 2024;10(19):e38303. doi:10.1016/j.heliyon.2024.e38303.
13. Prince HA, Ghosh A, Siam MMH, Mamun MAH. AI predicts MHD double-diffusive mixed convection and entropy generation in hybrid-nanofluids for different magnetic field inclination angles by ANN. Int J Thermofluids. 2023;19(9):100383. doi:10.1016/j.ijft.2023.100383.
14. Dhanraj T, Eswara Rao M, Vajravelu K, Lakshminarayana P. Analysis of carbon nanotubes-based nanofluid with paraffin oil in 3D MHD Darcy-Forchheimer flow through a bi-directional stretchable surface: application to heat exchanger systems. Proc Inst Mech Eng Part E J Process Mech Eng. 2026;240(2):1806–17. doi:10.1177/09544089241259446.
15. Karthik S, Iranian D, Alhazmi H, Khan I, Singh A, Khan MI. Double diffusive on Powell Eyring fluid flow by mixed convection from an exponential stretching surface with variable viscosity/thermal conductivity. Case Stud Therm Eng. 2024;55:104091. doi:10.1016/j.csite.2024.104091.
16. Guedri K, Hussain SM, Ahmad H, Abd-Elmonem A, Al-lehaibi M, Rehman S, et al. Heatline analysis of magnetic lid-driven radiated nanofluids flow via trapezoidal cavity in porous media. J Radiat Res Appl Sci. 2025;18(3):101805. doi:10.1016/j.jrras.2025.101805.
17. Hussain SM, Parveen R, Katbar NM, Rehman S, Abd-Elmonem A, Abdalla NSE, et al. Entropy generation analysis of MHD convection flow of hybrid nanofluid in a wavy enclosure with heat generation and thermal radiation. Rev Adv Mater Sci. 2024;63(1):20240037. doi:10.1515/rams-2024-0037.
18. Jalili B, Zar PM, Liu D, Ji CH, Jalili P, Abdelmohimen MAH, et al. Thermal study of MHD hybrid nano fluids confined between two parallel sheets: shape factors analysis. Case Stud Therm Eng. 2024;63:105229. doi:10.1016/j.csite.2024.105229.
19. Roshani H, Jalili P, Jalili B, Ahmad I, Hendy AS, Ali MR, et al. The effect of magnetic field on the heat transfer in the porous medium octagonal cavity with Cassini oval barriers. Case Stud Therm Eng. 2024;56:104194. doi:10.1016/j.csite.2024.104194.
20. Pandey S, Park YG, Ha MY. An exhaustive review of studies on natural convection in enclosures with and without internal bodies of various shapes. Int J Heat Mass Transf. 2019;138:762–95. doi:10.1016/j.ijheatmasstransfer.2019.04.097.
21. Hasan N, Saha S. Effects of internal heat production and Joule heating on MHD conjugate mixed convection and entropy production inside a thermally non-homogeneous cooling system. Ann Nucl Energy. 2024;206(6):110671. doi:10.1016/j.anucene.2024.110671.
22. Rupam MTI, Hasan N, Rasel MS, Saha S. Magnetohydrodynamic conjugate mixed convection, Joule Heating, and entropy generation through a ferrofluid filled T-shaped open miniature chamber with a Heat-Generating circular rod. Ann Nucl Energy. 2025;216(1):111294. doi:10.1016/j.anucene.2025.111294.
23. Aich W, Hilali-Jaghdam I, Alshahrani A, Maatki C, Alshammari BM, Kolsi L. CFD study and regression analysis of the MHD mixed convection of CNT-water nanofluid in a vented rounded edge rectangular cavity having inner vertical rod bundle. Mathematics. 2024;12(23):3677. doi:10.3390/math12233677.
24. Daneshvar Garmroodi MR, Ahmadpour A, Talati F. MHD mixed convection of nanofluids in the presence of multiple rotating cylinders in different configurations: a two-phase numerical study. Int J Mech Sci. 2019;150:247–64. doi:10.1016/j.ijmecsci.2018.10.037.
25. Wang Z, Wang T, Xi G, Huang Z. Periodic unsteady natural convection in square enclosure induced by inner circular cylinder with different vertical locations. Int Commun Heat Mass Transf. 2021;124:105250. doi:10.1016/j.icheatmasstransfer.2021.105250.

26. Xu HT, Wang ZY, Karimi F, Yang M, Zhang YW. Numerical simulation of double diffusive mixed convection in an open enclosure with different cylinder locations. Int Commun Heat Mass Transf. 2014;52:33–45. doi:10.1016/j.icheatmasstransfer.2014.01.005.
27. Souayeh B, Barhoumi Y, Ben-Beya B. Optimization of the heating of a cubic swimming Pool by a spherical heating block under a set of control parameters. Int Commun Heat Mass Transf. 2025;162:108625. doi:10.1016/j.icheatmasstransfer.2025.108625.
28. Souayeh B. Thermal performance analysis of oriented MHD convective flow and entropy production of hybrid nanofluids in a cavity induced by semicircles at different radii ratios. ZAMM J Appl Math Mech/Z Für Angew Math Und Mech. 2024;104(9):e202400015. doi:10.1002/zamm.202400015.
29. Souayeh B, Hammami F, Hdhiri N, Alam MW, Yasin E, Abuzir A. Simulation of natural convective heat transfer and entropy generation of nanoparticles around two spheres in horizontal arrangement. Alex Eng J. 2021;60(2):2583–605. doi:10.1016/j.aej.2021.01.002.
30. Souayeh B, Hdhiri N, Alam MW, Hammami F, Alfannakh H. Convective heat transfer and entropy generation around a sphere within cuboidal enclosure. J Thermophys Heat Transf. 2020;34(3):605–25. doi:10.2514/1.t5960.
31. Patankar SV. A calculation procedure for two-dimensional elliptic situations. Numer Heat Transf. 1981;4(4):409–25. doi:10.1080/01495728108961801.
32. Maxwell Garnett JC. Colours in metal glasses and in metallic films. Philos Trans R Soc Lond Ser A Contain Pap A Math Phys Character. 1904;203(1904):385–420. doi:10.1098/rsta.1904.0024.
33. Brinkman HC. The viscosity of concentrated suspensions and solutions. J Chem Phys. 1952;20(4):571. doi:10.1063/1.1700493.
34. Begum AS, Nithyadevi N, Öztop HF, Al-Salem K. Numerical simulation of MHD mixed convection in a nanofluid filled non-darcy porous enclosure. Int J Mech Sci. 2017;130:154–66. doi:10.1016/j.ijmecsci.2017.06.008.
35. Nithyadevi N, Shamadhani Begum A, Oztop HF, Abu-Hamdeh N. Mixed convection analysis in heat transfer enhancement of a nanofluid filled porous enclosure with various wall speed ratios. Int J Heat Mass Transf. 2017;113:716–29. doi:10.1016/j.ijheatmasstransfer.2017.05.134.
36. Thirumalaisamy K, Sivaraj R, Reddy AS. Fluid flow and heat transfer analysis of a ternary aqueous Fe_3O_4 + MWCNT + Cu/H_2O magnetic nanofluid in an inclined rectangular porous cavity. J Magn Magn Mater. 2024;589(7):171503. doi:10.1016/j.jmmm.2023.171503.
37. Ben Beya B, Lili T. Transient natural convection in 3D tilted enclosure heated from two opposite sides. Int Commun Heat Mass Transf. 2009;36(6):604–13. doi:10.1016/j.icheatmasstransfer.2009.02.014.
38. Ben Beya B, Lili T. Three-dimensional incompressible flow in a two-sided non-facing lid-driven cubical cavity. Comptes Rendus Mécanique. 2008;336(11–12):863–72. doi:10.1016/j.crme.2008.10.004.
39. Hayase T, Humphrey JAC, Greif R. A consistently formulated QUICK scheme for fast and stable convergence using finite-volume iterative calculation procedures. J Comput Phys. 1992;98(1):108–18. doi:10.1016/0021-9991(92)90177-Z.
40. Brown DL, Cortez R, Minion ML. Accurate projection methods for the incompressible navier-stokes equations. J Comput Phys. 2001;168(2):464–99. doi:10.1006/jcph.2001.6715.
41. Ghia U, Ghia KN, Shin CT. High-resolutions for incompressible flow using the navier-stokes equations and a multi-grid method. J Comput Phys. 1982;48(3):387–411. doi:10.1016/0021-9991(82)90058-4.
42. Ghasemi B, Aminossadati SM, Raisi A. Magnetic field effect on natural convection in a nanofluid-filled square enclosure. Int J Therm Sci. 2011;50(9):1748–56. doi:10.1016/j.ijthermalsci.2011.04.010.